# Studying of Geomagnetic Variations by Using Quartz Sensors

Dissertation

Submitted for the award of the degree of

*Master of Philosophy*

in

*Physics*

by

**Sheikh Ansar Hussain**

Under the Supervision of

**Dr. Gowher Bashir**

Department of Physics,

**University of Kashmir, Srinagar, 190006**

**December, 2012**

# Acknowledgments

First of all, my thanks goes to Almighty Allah, the most beneficial and merciful. After that, I would like to express deep sense of indebtedness and gratitude to my supervisor, **Dr. Gowher Bashir** for his enlightened guidance, untiring keen interest, patient help and const encouragement during my entire M. Phil. Work. Without his support and encouragement this work could not have been initiated. The long hours I had spend in his company were tough, but very productive.

I would like to thank Head of Department of Physics Professor **Sheikh Javid Ahmad** and other teachers of the department, who directly or indirectly supported me during my M. Phil. Work.

I have no words to express heartiest gratitude to my family members for their patience, blessings, encouragement and bearing with me throughout my M. Phil. Programme.

Finally thanks to all those who always wished successful academic carrier for me and also for their direct or indirect help, encouragement and enthusiasm.

**Sheikh Ansar Hussain**

# Post Graduate Department of Physics,

# University of Kashmir, Srinagar.

## Certificate

This is to certify that the dissertation entitled **"Studying of Geomagnetic Variations by Using Quartz Sensors"** submitted by **Sheikh Ansar Hussain**, in partial fulfilment for the award of the degree of ***Master of Philosophy*** in ***physics,*** is the original research work carried out by him under our supervision and guidance. It is further certified that the dissertation has not been submitted for award of M. Phil. Or any other degree to this university or any other university. The scholar has attended the department for statutory period as required under rules.

**Dr. Gowher Bashir** (*Supervisor)*

**Professor Sheikh Javid Ahmad** (*Head of the Department*)

# Contents

# Chapter 1

## Introduction

Natural events like Earthquakes, Tsunamis and Volcanic eruptions are inevitable. What makes these events more dangerous is not that these events are inevitable but these are still unpredictable. Therefore it is one of the major challenges felt presently by scientific community world over to find a reliable seismic precursors. The researchers have started efforts in this direction a couple of years ago. The studies carried out in the past using traditional seismological methods [1] have solved the long term prediction to a much extent. However the problem of short term prediction remains yet unsolved. Although the field of short term prediction is in its initial stages of study, yet precursors do exist and can be observed for forecasting earthquakes. In case of an earthquake rupture, certain precursory activity can be expected, if the observation is made in the near vicinity of causative rupture. These precursory activities may include; radio and helium emanation; electromagnetic emissions; water level and temperature changes; ground uplift and tilt; changes in ionospheric parameters and so on.

Among all earthquake precursors, those related to electromagnetic effects are most important as well as puzzling. The interest in electromagnetic phenomena caused by lithosphere and related to earthquake preparation increased considerably during the last ten years. The case studies have shown that these can be most promising tools for earthquake prediction. The subjective study of seismo-electromagnetism refers to electric and magnetic field anomalies [2] observed during seismicity. Recent studies have shown that these pre-seismic electromagnetic emissions occur in wide frequency band ranging from few mHz to few MHZ.

## 1.1 History

Global efforts to predict earthquake were started about a century ago and peaked during 1970s. The first scientifically well documented earthquake prediction was made on the basis of temporal and spatial variation of ts/tp relation in Blue mountain Lake, New York on 3rd August, 1973[3]. Seismologists then successfully predicted the Heicheng China earthquake of February 4, 1975, which raised the hopes that it could be possible to make reliable earthquake forecasts. The seismologists have now narrowed down their studies from long term predication to short term predication. The studies carried out in the past two decades have given birth to the new field of seismo-electromagnetism. Several enthaustic research groups all over the world have shown evidences of electromagnetic emissions and anomalies before earthquakes [4] first observed electromagnetic signals in the frequency range of 1-7MHz on applying stress to certain quartz bearing rocks and other piezoelectric materials.[5] reported that stressed rocks emitted electromagnetic and acoustic waves when micro fracturing took place. In 1980 electromagnetic wave was first observed at Sugadaira (Japan) before a large earthquake[6]. After this observation, electromagnetic waves associated with earthquakes have been reported by many researchers[7][8]. Such emissions have been found to normally account between ultra low frequency (ULF) and high frequency (HF) range. However the frequency band in ultra low frequency (ULF) range (0.01-10Hz) has been found to yield more reliable precursors because of their large skin depth and low attenuation [9] .The generation mechanisms of ULF emission prior to a seismic event is possibly related to fracturing processes like piezoelectric effects, electro kinetic effects and turboelectric effect. The ULF emissions can penetrate the crust and propagate through ionosphere and magnetosphere [10][11], hence are easily recorded by ground and space based systems. Moreover these emissions occur few hours to few days before the main shock and their presence is felt even after the main shock for an inconsistent time

period. Hence these ULF/ELF emissions could be used as short term precursors in the area of earthquake prediction[12]. Although very low frequency emissions have also been detected in the range of 500-3600Hz before Koguelen Island earthquake [13]. However, scientists have been most attracted by ULF range, because there have been convincing evidences on precursory occurrence of such emissions before large earthquakes like Spitak [14], Loma Pieta [15], Guam[16] . These effects have also been recently reported [17][18][19][20][21] have reported that precursory time of such emissions can be from few days to several weeks. These experimental evidences have been positively supported by the theoretical work, wherein efforts have been made to explain their generation mechanisms[22].On the other hand some models discussing the conditions prior to dynamical main shock have been proposed [23] . The Plasmon model [24] suggested that by increase of strong stress on the rocks, exoelectron are excited and emitted and bulk Plasmon into photon (EM wave).

Recently efforts have been made to utilize ULF data for direction finding of emitted signals from epicentre regions [25] . [26] Found that ULF emission can be observable within the epicentral distance of- 100Km for an earthquake of magnitude 7 while -70-80 Km for an earthquake of magnitude 6. However long distance propagation of ULF emissions has also been reported by [27] and [28]. [29] found that seismic associated ULF emissions are accompanied by an additional signal which differentiates them from non-seismic ones. The additional signal appears only few days before the earthquake and its horizontal magnetic field is more linear and rotated towards meridonal direction. The difference being clearly visible in polarization parameters than in spectral power with maximum effect at frequencies between Schumann resonances. The unusual enhancement in magnetic field components prior to seismicity has also been reported.

Japanese and French institutes have developed network of observatories to completely monitor pre-seismic emissions and highly advanced methods and techniques to process the data [30] . More recently other aspects associated with

Seismogenic ULF/ELF emissions are being evaluated with the help of LEO (Low earth orbiting) Satellites. Among the different precursory phenomenon mentioned in the publications on earthquake prediction, the ionospheric ones are youngest. It has been now established that ionosphere is not only sensitive to solar influences, but it is also affected by lithospheric processes. The occurrence of some specific phenomenon at different altitudes and in different layers of ionosphere is believed to be caused by lithospheric processes happening prior to a seismic event. The researchers are of the view that there is a perfect connection between lithosphere and ionosphere, which may be established either from ground or from space. Above the epicentre of future earthquake, there appears a macroscopic change in the ionospheric parameters at an altitude between 400Km to 1000Km.

In recent years, the existence of ionospheric precursors of earthquakes has attracted much attention of space physics research community [31] and [32] . There are many evidences of seismic associated ionospheric disturbances [33] and [34] . The first publication concerning seismic associated ionospheric effects came just after Alaska "Good Friday" earthquake in 1964 [35] and[36]. Since then a wide range of ionospheric-seismogenic phenomena has been acquired by in-situ satellite and ground based measurements. Using data of ground based ionosondes[37] studied variation of foE parameter before Tashkent earthquake. In 1985 [38] reported increase in foF2 two days before the main shock while [39] reported a decrease in foF2 before the main shock. Similar results have been obtained by[40] and [41] . Satellites have registered specific variations and plasma disturbances associated with earthquakes[42][43] . In addition the plasma density, ion composition was also analyzed and reported[44] .

Ionospheric perturbations linked with earthquakes have also been studied extensively by number of researchers[45][34][46]. These are due to propagation of acoustic gravity waves which interact with ionosphere as suggested by first seismo-ionosphere coupling mechanism[47][48]. Attempts have also been made to study and

establish lithosphere-ionosphere coupling [49] [50] [51] .Total Electron Content (TEC) from GPS has also proved to be useful tool in studying ionospheric effects associated with earthquakes [41][52] . It has been found that smooth variation in TEC is replaced by rapid fluctuations during seismicity. Ground based measurements of ionosphere perturbations. Associated with seismic activity have also been done with ionosondes [53][43][54].

The successful launch of DEMETER satellite by French agency CNES (French National Space Agency) in 2004 was a big landmark in the history of earthquake physics. The satellite is a dedicated mission to monitor seismo-ionospheric perturbations. The satellite has proved an extensive database to study ionospheric disturbances during earthquakes. [12][13] Have been continuously using DEMETER data since its launch to study electromagnetic emissions and associated ionospheric perturbations linked to seismic activity.

## 1.2 Recent results

There have been reported three reliable events for the ULF magnetic field variations prior to the earthquakes; (1) Armenia, Spitak earthquake (1988 December 8, Magnitude=6.9)[55], (2) USA, California, Loma Priesta earthquake (1989 October 18, M=7.1) [56], and (3) Gauam earthquake (1993 August 8, M=8.0) [57]. The epicentral distance is 129 Km for (1), 7 Km for (2) and 65 Km for (3) [58][59]. The Loma Priesta earthquake happened very close to the observing station, so it is better for us to indicate the results for this earthquake. Fig.1.1 illustrates the temporal evolution of ULF magnetic field (horizontal component, frequency=0.01 Hz (period = 100 s) ).It indicates that the magnetic field increases for about one week 5-12 days before the earth quake, followed by a quite period and a sharp increases one day before the earthquake (especially an abrupt increase 3-4 hours before the earthquake). Very significant changes in ULF magnetic field were also observed for other two earthquakes, which was a stimulus to the extensive research on the relationship of

ULF emission and earthquakes. An addition important point is that these seismogenic ULF emissions are so weak.

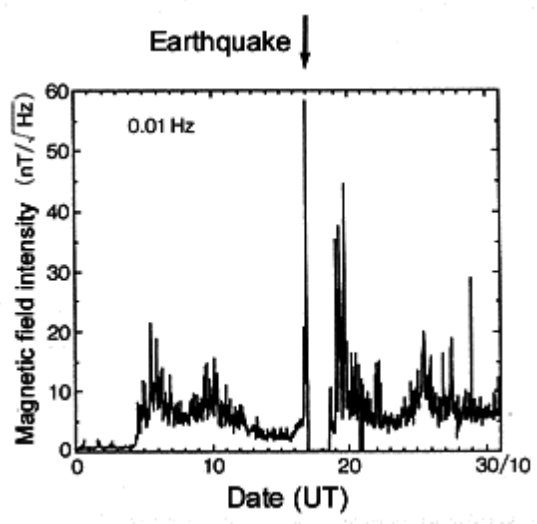


**Figure 1.1:** Temporal evolution of geomagnetic variation for the Loma Prieta earthquake (f=0.01Hz).

## 1.3 Plan of Dissertation

In the second chapter, I had discussed the geomagnetic variations, their types and causes of these geomagnetic variations. Temporal changes in the geomagnetic field, both long-term (secular) and short-term (transient) are called as geomagnetic variations. Then, I have discussed the Short-term geomagnetic variations, those variations in which the geomagnetic field varies on the time scale from second to milliseconds. These variations generally arise from ionosphere (ionospheric dynamo region) and magnetosphere, and some changes can be traced to geomagnetic storms or daily variations in currents. Changes over time scales of a year or more mostly reflect changes in the Earth's particularly the iron-rich core. Long term or secular variations are the changes in the magnetic field on the time scale of a year or more. In

the same chapter I have also discussed the different types of waves that are generated during earthquakes i.e. is Seismic waves. They are of two types body waves and surface waves. Body waves travel through the interior of earth. Compression waves or P-waves are its first type, the second type of body waves are secondary or S-waves. These are transverse in nature. The second type of seismic waves is surface waves. These waves travel through the crust of earth. The first kind of surface waves are Love or L-waves, they are transverse in nature. The second type of surface waves are Rayleigh waves. The conventional seismic observations provide us with macroscopic information of the lithosphere, particularly after the occurrence of an EQ, which contribute much to the understanding of the mechanisms of EQ generation, but is no contribution to EQ predication.

Then I have discussed the non seismic electromagnetic emission and the possible physical mechanisms which are responsible for their generation. These microscopic effects of the lithosphere would provide us with the useful information for EQ predication. As increase in the pressure just around the hypocentre would always accompany micro-fractures, leading to the change separation and generation of currents, which would be essential source of subsequent electromagnetic effects. One of the electromagnetic effects generated are em waves, which can propagate over relatively long distances, of course depending on the wave frequency. These two factors (precursory and the long distance propagating nature) of the electromagnetic effects are decively advantageous over the former conventional seismic measurements. We will concentrate on ULF electromagnetic emissions. The ULF emission is a direct consequence of the lithosphere.

The different types of physical mechanisms which produce the electric, magnetic and electromagnetic disturbances apparently associated with earthquakes and volcanic eruptions are Piezomagnetism, stress/conductivity, electrokinetic effects, charge generation processes, charge dispersion, magnetohydrodynamic effects, and thermal magnetization and demagnetization effects. In the second chapter, I have also

discussed these effects in detail. In the same chapter we will also discuss ULF geomagnetic changes due to ULF emissions.

In the third chapter we have give a detailed description of different types of magnetometers. Actually magnetometers are of two types 1: scalar magnetometers, the different types of scalar magnetometers are proton pression, Overhauser, and a range of Alkali vapour instruments including Caesium, Helium and Potassium. 2: vector magnetometers, Examples of vector magnetometers are fluxgates, superconducting quantum interference devices (SQUIDs), and the atomic SERF magnetometer. Then in the same chapter we have discussed Quartz and its properties.

In the fourth I have discussed recording of magnetic field and different types of analysis methods ,these include cumulative Probability Plots, Polarization analysis, Principal Component analysis, Inter-station transfer function (ISTF) method, Direction Finding, Magnetic Field Gradient Method, Goniometric Method, A new Polarization Ellipse Method, Polarization Ellipse and Direction Finding and Fractal Analysis.

In the last chapter I have discussed Characteristics of Seismogenic ULF emission and future direction on network of magnetic field observations. In conclusion I have discussed that we will establish an efficient network in Jammu and Kashmir which will consists of highly efficient magnetometers and sensors. This would enable us to accumulate the number of events as well. Then we will use highly sophisticated signal processing's to identify the ULF signals.

# Chapter 2

## The magnetic field of earth

It is believed that the earth was formed by accretion of pyrolite, chrondrites and other kind of meteorite substances, which after radioactive heating and compression melted fractionally to give the basaltic magma leaving behind dunite-periodotite type rocks. The geomagnetic field is supposed to be created by a self-excited dynamo action firstly due to convection in the liquid core caused perhaps by heating due to radioactive materials and secondly due to a possible differential rotation of the liquid core1.The actual validity of such a mechanism is by no means established and much further investigation is necessary.

The magnetic field of the earth observed all over the globe is a vector field. Three components of the vector F are needed to describe the field. The usual components recorded or observed are plotted in fig 2.1

In fig 2.1 X= North component of the vector F, Y= East component of the vector Z=Vertical component of the vector F(positive down) called vertical intensity, H= horizontal intensity or the horizontal component of vector F along magnetic meridian (positive direction towards the north), D=magnetic declination or the angle(positive east) between the geographic north direction and the magnetic meridian (angle between X and H ), and I= magnetic inclination or the angle between the horizontal intensity vector (H) and the magnetic field vector of total intensity(f). I is positive downward.

William Gilbert (1600) deduced from observations made at different latitudes that the Earth's magnetic field is similar to that of magnetized sphere. His conclusion was that the earth is a spherical magnet. Later, more detail observations showed that the field at the earth's surface roughly resembles the field of the magnetic dipole placed

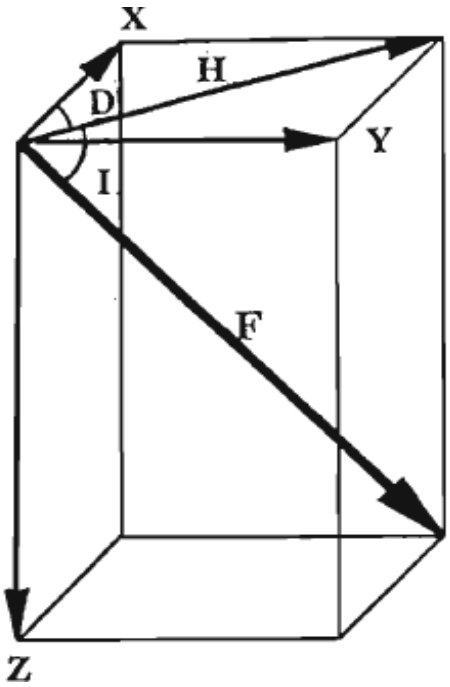


**Figure 2.1**

The formulas showing relations between the components in Figure 2.1 are

$$F^2 = X^2 + Y^2 + Z^2 = H^2 + Z^2;$$

$$H^2 = X^2 + Y^2;$$

$$X = H\cos D;$$

$$Y = H\sin D = X\tan D;$$

$$Z = F\sin I = H\tan I;$$

$$D = arc\tan\left({}^{Y}/_{X}\right);$$

$$I = arc\tan\left({}^{Z}/_{H}\right);$$

Close to the earth's centre and tilted $11.5^0$From the rotation axis of the earth.More than 90% of the observed field can be approximatedby this simple dipole model.Today we know that the field of magnetized sphere is similar to the field of a magnetic dipole placed at the centre of the sphere. We know that the hypothesis of a magnetized sphere cannot be right because the iron in the rocks cannot be magnetized at temperatures higher than the Curie point, which is exceeded at a depth of a few tens of kilometres.

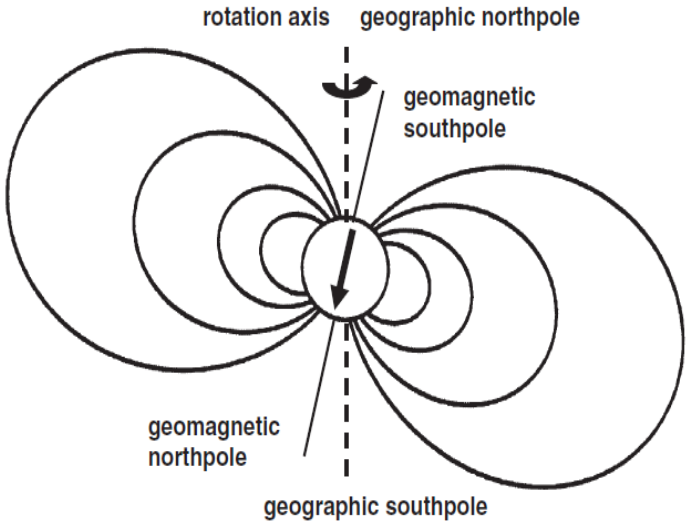


**Figure 2.2:** Geocentric dipole and its field lines. The dipole axis is tilted about $11.5^0$With respect to the axis of rotation.

According to the present explanation, the so called hydro magnetic dynamo theory, the main part of the Earth's magnetic field arises from electrokinetic currents is about 2900km. The field at the earth's surface due to these currents is about 30000nT at the equator and 60000nT in polar areas. The current systems in the core do not seem to be stable and homogeneous. Therefore the field measured at the Earth's surface

shows large anomalies compared to a dipolar field. These regional magnetic anomalies have dimensions of thousands of kilometres and are caused mainly by the in homogeneity of the electric currents inside the earth. The non-uniform distribution of Magnetic minerals in the Earth's crust is also seen as smaller scale anomalies in the otherwise smooth field. These local anomalies can be strong, several tens of thousands of nT.

## 2.1 Secular variations

The main field of the earth is that part of the field which has its origin in the core. The change of the main field is called secular variation, which well describes the slow character of the variation. For the slower field variations, data for the last two or more centuries show. The geomagnetic field has been predominantly dipolar with the dipolar axis and the axis of the earth roughly coincident.

The main dipole component has maintained an approximately constant direction over several decades. However the magnitude of the total magnetic dipole moment has reduced from about 8.5 in 1833to about 8.0($\times 10^{25} G\ cm^{-3}$) in 1965, indicating a rate of change of about 5% per century. if this rate continues, the present geomagnetic field should reduce to zero in 1400 A.D. changes for 1964-70 are given in2

(1) The non–dipole component shows a considerable secular variation. The electric dipole has moved northwards and westwards since 1835 drifting about 0.1.

(2) Power spectrum analysis has revealed periodicities of about 11, 17, 22, 60 and perhaps 80 years.

(3) Changes in the declination (D)and the inclination(I) of the of the geomagnetic field for the last several thousand years indicate possible periodicities of 400,700, 1200, 1800 and 8000 years.

## 2.2 Seismic waves

Seismic waves are the waves of energy caused by the sudden breaking of rock within the earth or an explosion. They are the energy that travels through the earth and is recorded on seismographs.

There are several different kinds of seismic waves, and they all move in different ways. The two main types of waves are body waves and surface waves. Body waves can travel through the earth's inner layers, but surface waves can only move along the surface of the planet like ripples on the water. Earthquakes radiate seismic energy as both body and surface waves.

## 2.3 Body waves

Travelling through the interior of the earth, body waves arrive before the surface waves emitted by an earthquake. These waves are of higher frequency than surface waves.

### 2.3.1 P Waves

The first kind of body waves is P waves or body waves. This is the fastest kind of seismic wave, and, consequently, the first to 'arrive 'at a seismic station. The P wave can move through solid rock and fluids, like liquid layers of the earth. It pushes and pulls the rock it moves through just like sound waves push and pull the air. Sometimes animals can hear the P waves of the earthquake .Dogs, for instance, commonly begin barking hysterically just before an earthquake 'hits'

P waves are also known as compression waves, because of the pushing and pulling they do. Subjected to a P wave, particles move in the same direction that the wave is moving in, which is the direction that the energy is travelling in, and is some-

times called the ‘direction of wave propagation’. Speed of P wave is given by:

$$\alpha = \sqrt{\frac{x+\frac{4}{3}\mu}{\rho}}$$

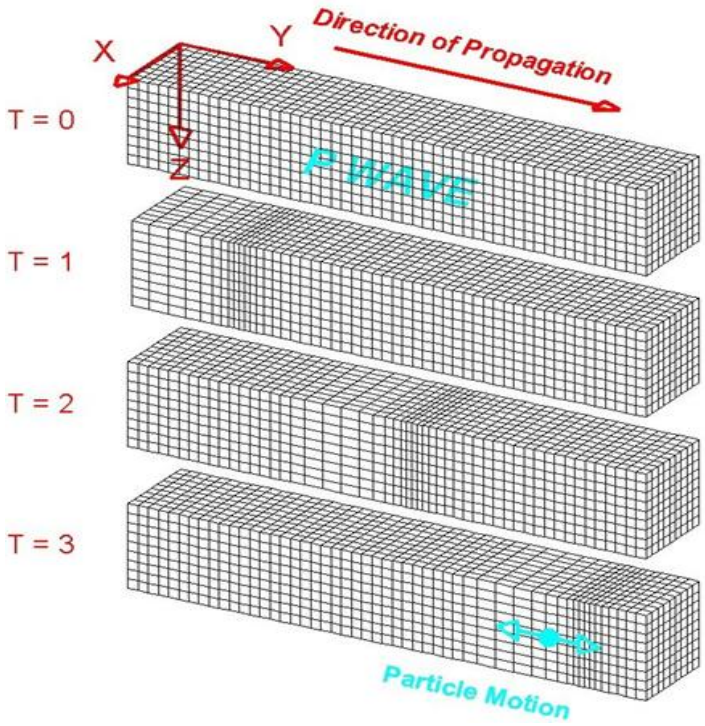


**Figure 2.3.1:** A P wave through a medium by means of compression and dilution. Particles are represented by cubes in this model.

## 2.3.2 S waves

The second type of body waves is the s waves or secondary waves, S waves are transverse in nature, because they move rock particles up and down or side-to-side perpendicular to the direction of propagation. These are also called ‘shear ‘waves

because they don't change the volume of the material through which they propagate, they shear it. The S wave move slower than a P wave and can only move through solid rocks, not through any liquid medium. It is this property of S waves that lead seismologists to conclude that the earth's outer core is a liquid. The s-wave speed, call it $\beta$, depends on the shear modulus and the density.

$$\beta = \sqrt{\frac{\mu}{\rho}}$$

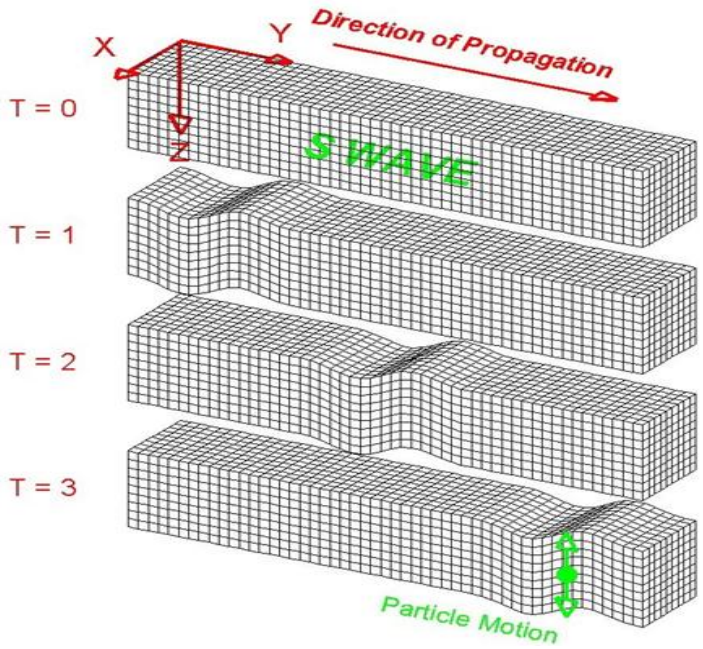


**Figure 2.3.2:** An S wave travels through a medium. Particles are represented by cubes in this model.

Typical S-wave propagation speeds are of the order of 1 to 80 km/sec. In genera earthquakes generate large shear waves than compression waves and much of the damage close to an earthquake is the result of strong shaking caused by shear waves.

## 2.4 Surface waves

Travelling only through the crust, surface waves are of lower frequency than body waves, and are easily distinguishable on a seismogram as a result. Though they arrive after body waves, it is surface waves that are almost entirely responsible for the damage and destruction associated with earthquakes. This damage and the strength of the surface waves are reduced in deeper earthquakes. They are of two types: 1.love waves 2.rayleigh wave.

### 2.4.1 Love waves

The first kind of surface waves is called a Love wave, named after A.E.H. Love, a British mathematician. Love waves are transverse waves that vibrate the ground in the horizontal direction perpendicular to the direction that the wave is travelling. They are formed by the interaction of S waves with Earth's surface and shallow structure and are dispersive waves. The speed at which a dispersive wave travels depends on the wave's period. In general, earthquake generates Love waves over a range periods from 1000 to a fraction of a second, and each period travels at a different velocity but the typical range of velocities is between 2 and 6 Km/second. Figure 2.4.1 shows a Love travels through a medium. Particles are represented by cubes in this model.

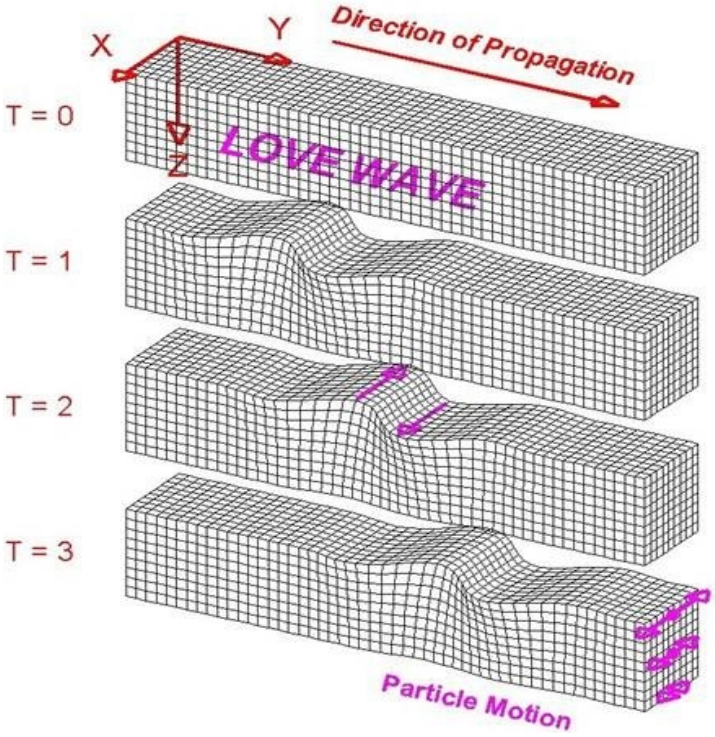


**Figure 2.4.1:** shows a Love travels through a medium Particles are represented by cubes in this model.

## 2.4.2 Rayleigh Waves

The other kind of surface wave is the Rayleigh wave, named after John William, Lord Rayleigh, who mathematically predicted the existence of this kind of wave in 1885.A Rayleigh wave rolls along the ground up and down, and side-to –side in the same direction that the wave is moving. Like Love waves they are dispersive so that the particular speed at which they travel depends on the wave period and the near-surface geologic structure, and they also decrease in amplitude with depth. Typical speeds for Rayleigh waves are of the order of 1 to 5 Km/s. Figure 4 shows a Rayleigh wave travels through a medium. Particles are represented by cubes in this model.

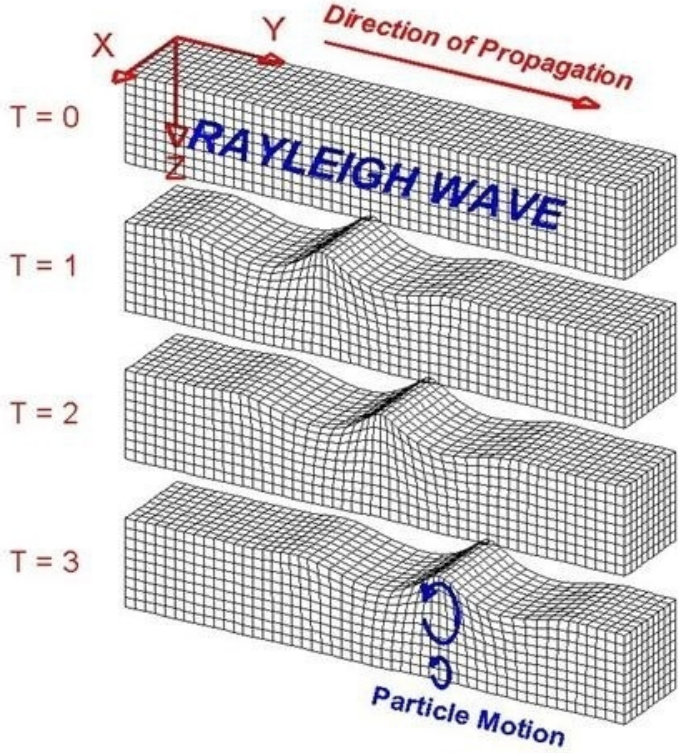


**Figure 2.4.2:** shows a Love travels through a medium. Particles are represented by cubes in this model.

## 2.5 Summary of physical Mechanisms Involved in ULF Emissions

The loading and rupture of water-saturated crystal rocks during earthquakes, together with fluid/gas movement, stress redistribution, and change in material properties, has long been expected to generate associated magnetic and electric field perturbations. The detection of related perturbations [58 – 81] prior to fault rupture has thus been proposed frequently as a simple and inexpensive method to monitor the state of crustal stress and perhaps to provide tools for predicting crustal failure. . The primary mechanisms for generation of electric and magnetic fields with crustal deformation and earthquake-related fault failure include Piezomagnetism, stress/conductivity, electrokinetic effects, charge generation processes, charge dispersion, magnetohydrodynamic effects, and thermal magnetization and demagnetization effects.

### 2.5.1 Electrokinetic effect

The role of active fluid flow in the earth's crust as a result of fault failure can generate electric and magnetic fields[82][83][70][72][74][80]. Electro kinetic electric and magnetic fields result from fluid flow through the crust in the presence of an electric double layer at the solid liquid interfaces. This double layer consists of ions anchored to the solid phase, with equivalent ionic charge of opposite sign distributed in the liquid phase near the interface. Fluid flow in this system transports the ions in the fluid in the direction of flow, and electric current results. Conservation of mass arguments [80]supported by surface strain observations[84] limit this process in extent and time because large-scale fluid flow cannot continue for very long before generating easily detectable surface deformation.

The current density J and fluid flow ν are found from coupled equations [85][70] given by

$$j = -s\nabla E - \frac{\varepsilon\zeta\nabla P}{\eta} \qquad 2.5$$

$$\nu = \frac{\emptyset\varepsilon\zeta\nabla E}{\eta} - \frac{\kappa\nabla P}{\eta} \qquad 2.6$$

Where E is streaming potential, s is the electrical conductivity of the fluid, $\varepsilon$ is the dielectric constant of water, $\eta$ is fluid viscosity,$\zeta$ is zeta potential, $\emptyset$ is porosity, $\kappa$ is the permeability, and p is pore pressure.

The current density in Eq. (2.5) has two components. The second term represents electric current resulting from mechanical energy being applied to the system and is sometimes called the "impressed'' current [86] This term describes current generated by fluid flow in fractures. The first term of eq. (2.5) represents back currents resulting from the electric field generated by fluid flow. The distribution of electric conductivity determines the net far-field magnetic and electric fields resulting from these effects. In an extreme case, if the fluid is extremely conducting and the surrounding region is not, current flow in the fluid cancels the potential generated by the fluid flow [87] . At the other extreme, if the fluid is poorly conducting, "back" currents, usually termed "volume currents" [86] flow in the surrounding region. If the region were homogeneous, magnetic fields would be generated by impressed currents only since the volume currents generate no net field [70][80] . The situation for finite flow in limited fault fractures more closely 8approximates the second case where the surface magnetic field is approximately given by:

$$A=\frac{\mu_0}{4\pi}\int\frac{j_1\times r}{r^2}dA \qquad 2.7$$

Where $\mu_0$ is the magnetic permeability in free space Note that the physics describing the electric and magnetic fields generated in the human body as blood is pumped through in arteries provides a very good analogue to those generated in

the faulty zones[86]. This occurs because the electrical conductivities of bone ($0.001 S m^{-1}$), muscle ($0.1\ S m^{-1}$) and blood ($1\ S m^{-1}$) and blood velocities are similar to those of rock, fault gouge, fault zone fluids, and the likely fluid velocities determined by Darcy Law fluid diffusion in fault zones. Considerable work has been done in understating the physics of electric and magnetic field generation in the human body and this can be applied directly to crustal faulting situations. Reasonable fault models, in which fluid flows into a 200m long rupturing fracture at a depth of 17km, indicates that transient surface electric fields of several tens of mill volts per kilometre and transient magnetic fields of a few nT can be generated [80].

## 2.5.2 Piezomagnetism

The magnetic properties of rocks have been shown under laboratory conditions to depend on the state of applied stress [58][88 – 94]. Theoretical models have been developed in terms of single domain and pseudo-single domain rotation [95][65][96] and multidomain wall translations[97][91][92] .The fractional change in the magnetization per unit volume as a function of stress can be expressed in the form;

$$\Delta I \approx K\sigma . I \qquad 2.8$$

Where $\Delta I$ is the change in magnetisation in a body with net magnetization I due to a deviatory stress $\sigma$. K, the stress sensitivity, typically has values of about $3 \times 10^{-3} MPa^{-1}$. The stress sensitivity of the induced and remnant magnetisation from theoretical and experimental studies has been combined with stress estimations from dislocation models of fault rupture and elastic pressure loading in active volcanoes to calculate magnetic field changes expected to accompany earthquakes and volcanoes [60][61][98][99][100][101][76][102][103][104].

The surface fields($\Delta B_p$) at a point P, can be calculated in two ways: (1) by either integrating the change in magnetisation $\Delta I_Q$ in a unit volume, dv, at a point Q Where the stress is $\sigma_{ij}$, and r is the distance between P and Q according to,

$$\Delta B_p = -\frac{\mu}{4\pi} \nabla \int \Delta I_Q . \frac{r}{r^3} d \qquad 2.9$$

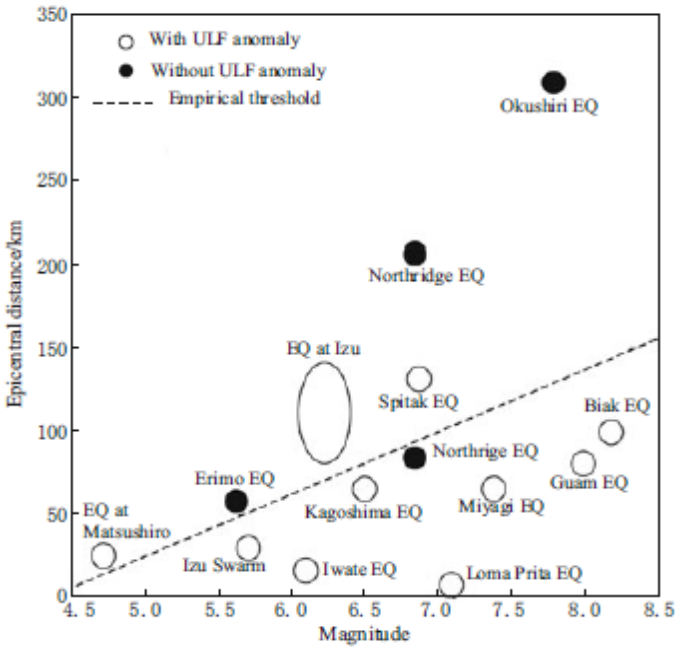


**Figure 2.5:** Summary of the seismogenic ULF emissions in the form of EQ magnitude (M) and epicentral distance(R). A open circal means the event with ULF anomaly, while a soild circle, the event without ULF anomaly. The empirical threshold is indicated by a dashed line ($0.025\,R \leq M - 4.5$)

As orginally done by [60],or (2) by using a simpler method pioneered by [75][105] in which analytic expressions of the surface Piezomagnetism potential, W, produced by a known stress distribution in a magneto elastic halt-space are obtained by transfo-

rming the stress matrix and integrating over the magnetised region. In this latter case, the surface field can be found from:

$$\Delta B_p = -\nabla W \qquad 2.10$$

These models show that magnetic anomalies of a few nanoteslas (nT) should be expected to accompany earthquakes for rock magnetizations and stress sensitivities of 1 ampere/meter ($Am^{-1}$) and $10^{-3}MPa^{-1}$, respectively. As shown below, these signals are readily observed with the correct sign and amplitude.

## 2.5. Stress/Resistivity and Strain/Resistivity effects

In a like manner, the stress dependence of electrical resistivity of rocks has been demonstrated in the laboratory. Resistivity in low porosity crystalline rock increases with compression as a result of crack closure at about 0.2%/bar[106] and decreases with shear due to crack opening at about 0.1%/bar[62][63][64][107]. More porous rocks have even lower stress sensitivity. The situation is even complicated by the fact that non linear can also produce resistivity changes[108] . A stress/resistivity relation equivalent of equation1 has the form

$$\frac{\Delta\rho}{\rho} \approx k_r \sigma \qquad 2.11$$

For homogeneous material, where $\rho$ is resistivity, $k_r$ is the constant, and $\sigma$ is the stress.Unfortunately, the earth is not homogeneous and many factors including rock type, crack distribution, degree of saturation, porosity, strain level, etc., can localize or attenuate current flow. Nevertheless, this equation provides a starting point of calculating resistivity changes near active faults. Measurements of resistivity changes are being made with both active experiments(where low frequency currents are injected into the ground and potential differences, V, are made on receiver dipoles),

or passive telluric and magnetotellurics(MT)experiments where changes in resistivity are inferred from changes in telluric or MT transfer functions. These transfer functions are given by:

$$Z(\omega) = \frac{E(\omega)}{H(\omega)} \qquad 2.11$$

Where $\omega$ is angular frequancy, $\omega$ is the angular frequency,$E(\omega)$ and $H(\omega)$ are observed electric and magnetic fields. For active experiments[109]

$$\frac{\delta\rho}{\rho} = G\frac{\delta V}{V} \qquad 2.12$$

Where $\delta V$ is the change in potential difference and G is a constant. For MT experiments,

$$\delta\rho = \delta\frac{|Z(\omega)|^2}{\omega\mu} \qquad 2.13$$

Based on the field observations of stress changes accompanying earthquakes($\approx$ 1MPa), resistivity changes of at least 1% might be expected to accompany crustal failure. Field experiments for detection of resistivity changes thus need to have a measurement precision of better than 0.1% [110][78][109] .This may be difficult with MT measurements unless remote magnetic field reference measurements are used[111] although measurement pression for telluric electric fields can be made at the 0.1% level[112]

## 2.5.4 Charge Generations Process

Numerous charge generation mechanisms have been suggested as potential current sources for electric and magnetic fields before and during earthquakes and volcanic eruptions. These mechanisms include piezoelectric effects, [113][114] triboelectricty

effects produced by rock shearing [115 – 117] fluid disruption/vaporization [118 – 120] and soild state mechanisms[121][122] . Each of these mechanisms has a solid physical basis with support by laboratory experiments on dry rocks in insulating environments or single crystals of dry quartz. Each is capable of producing substantial charge under the right conditions. However, at least two fundamental need to be studied in the application of charge-generation processes to EM field generation in the Earth's crust. The first concerns the amplitude of each charge generation effects in wet rocks and the second concerns charge maintenance time and propagation in the conducting crust.

Regarding the first problem, experiments clearly need to be done for each mechanism to quantify the effects expected in wet rocks at temperatures of at least 100 C and at confining pressures of 100 MPa expected at earthquake hypocenters. Experiments on dry rocks at atmospheric pressure are not very relevant to this issue. Piezoelectric effects in dry quartz bearing rocks are less than 0.1% of those observed for single crystals of quartz due to self cancelling effects[123][124], and effects in wet rocks will likely be smaller still and transient at best. EM generation by fracturing dry rocks[125][117] needs to be extended to wet rocks under confining pressure. Experiments on hole transport of 0 in dry rocks[121] need also be repeated with wet rocks under confined pressure so that these effects can be quantified. [117] Observed no EM emission during fracture of conductive rocks since the conductor could not maintain charge separation.

The second fundamental problem concerns the discharge time for these processes and just how far EM signals generated by them might propagate. The charge relaxation time $\boldsymbol{\tau}$ for electrostatic processes is given by the product of permittivity ($\varepsilon$) and the resistivity ($\rho$). $\varepsilon$ is 0.5-1.0$\times$ $10^{-10}$ $Fm^{-1}$for crustal rocks. If $\rho \approx 10^3$ ohm.m (typicaly upper value for near fault crustal rock) then,

$$\tau \approx 10^{-6}\text{Sec} \qquad 2.14$$

Although polarization effects [126] will generate somewhat longer timescales (perhaps-

as much as a second), EM signal generation by charge generation processes must necessarily still be very rapid unless mechanisms can be found for isolating and maintaining large charge densities in a conducting earth. Furthermore, dispersion precludes EM fields propagating very far in a conducting earth [127].

Attenuation of the magnetic field, B, of a plane electromagnetic wave generated at depth by charge generation/cancellation processes as a function of penetration distance through a conductive medium is given by:

$$B = B_0 e^{-\gamma z} \qquad 2.15$$

Where $B_0$the intial field strength, z is is penetration distance into the medium, ϒ is the complex propagation coefficient given by:

$$\gamma = \sqrt{\omega^2 \mu\varepsilon + j\omega\mu s} \qquad 2.16$$

Where **ω** is the angular frequency of the radiation, $\mu$ is the magnetic permeability of the earth, ε is the permitivity and s is the conductivity of the medium. If these fields are generated by rock cracking and fracturing, acoustic (seismic) signals should be generated[128].Seismic wave attenuation with distance z has the form

$$A(z) = A_0 e^{-(\omega z/2cQ)} \qquad 2.17$$

Where ω is the angular frequency, c is the phase velocity, and Q is the quality factor. Taking observed values of 3 Km$sec^{-1}$ and 30 for c and Q, it can easily be shown that seismic waves in the frequancy band 1-0.01 Hz are not attenuated significantly in the epicentral area. At higher frequencies, both seismic and EM signals are heavily attenuated. For example, at 10Hz the EM "skin depth" is 493m in material with conductivity of 0.1 S$m^{-1}$and the seismic equivalent "pentration depth" is 2864m.At 100Hz the comparative depths are 156m, 286m, and at 1 KHz 29m, 49m, respectively.

Thus, both high frequency seismic and EM waves are heavily attenuated in the earth's crust. EM sources at 10Hz should have an acoustic component that is more easily detected over a greater area. In fact, for all EM sources at seismogenic depths capable of propagating to the earth's surface, acoustic/seismic consequences of these sources propagating more effectively to the surface and might be used to verify their existence.

## 2.5.5 Magnetohydrodynamic (MHD) Effects

The induced magnetic field $B_i$ generated by the motion ν of a fluid with conductivity s in a magnetic field$B_0$, is governed by the equation:

$$\frac{\partial B}{\partial T} = \nabla \times \nu \times B + \frac{\nabla^2 B}{\mu_0 S} + \frac{\nabla s \times \nabla \times B}{\mu_0 s^2} \qquad 2.18$$

Where $\mu_0$ is the permeability in vacuum[129]. For low magnetic fields and low electrical conductivities in the Earth's crust where the fluid motion is not affected by the induced fields, the induced field is given approximately by the product of the magnetic Reynolds number $R_m$ and the imposed field $B_0$, i.e.,

$$B_i \approx R_m \times B_0 \approx \mu s \nu d B_0 \qquad 2.19$$

Where d is the length scale of the flow. Critical parameters here are likely flow velocities and fluid electrical conductivities in the crust. Flow velocity is determined by rock permeability and fluid pressure gradients according to Darchy's Law. Permeability of fractured rock is not less than $10^{-12} m^2$[130] and pore-pressure gradients cannot exceed the lithospheric gradient. It is difficult to achieve widespread flow velocities of even a few millimetres $sec^{-1}$with this mechanism. Furthermore, fluid conductivities are unlikely to exceed that of sea water. Using these numbers, fluid flow in fractured fault zones at seismogenic depths (≈5Km) with a length scale of 1 Km could generate transient fields of about 0.01nT. This is far too small to be

observed at the earth's surface. As a check on these calculations, we note that fields of a few nT are observed with waves in the ocean where the conductivity is 1 S$m^{-1}$and wave velocities exceed 100 cm $sec^{-1}$[131].

## 2.5.6 Thermal Remagnetization and Demagnetization

Crustal rocks lose their magnetization when temperatures exceed the curie point ($\approx 580^0$ C for magnetite) and become remagnetized again as the temperature drops below this value. [132] describe this process in detail. In crustal rocks at seismogenic depths near active faults, this process is unlikely to contribute to rapid changes in local magnetic fields since the thermal diffusivity of rock is typically about$10^{-6}m^2sec^{-1}$ migration of the Curie Point isothermal by conduction cannot be as much as a meter in a year [133]. At shallow depths in volcanic regions, particularly recently emplaced extrusions, thermal cracking with gas and fluid movement can transfer heat rapidly and large local anomalies can be quickly generated[134][135][136][137][138][139][140][141][142] . These anomalies can be modedeled as a magnetized slab in a half-space. Good examples of magnetic modelling of anomalies generated by cooling of extractions can be found[139] for Mt. St. [142] for Mt. Unzen in Japan. Some seasonal variations may result from annual temperature diffusion into magnetic rocks in the upper few meters of earth's crust [14]

## 2.5.7 ULF Geomagnetic Changes Due To ULF Emissions

In the 1990's the idea that ULF emissions were associated with large earthquakes became apparent. This idea opened up possibilities for short term predication . Table 1 shows results from three pioneering works. ULF emission associated with large earthquakes was almost simultaneously discovered in Russia and America. The first recording of earthquake-related ULF emission was carried out by a Russian group. They reported anomalous ULF emission preceding the 1988 Spitak earthquake (M6.9). The second was a significant observation associated with the Loma Priesta earthquake [56]. Here, the epicentral distance was small and the focal depth where shallow resulting in the simple amplitude record showing an apparent anomalous change. Figure 4 shows the variation of magnetic intensity at 0.01 Hz (100 seconds period) band, which exhibits the first enhancesment from two weeks to 1 week prior to the earthquake, followed by a quit period, and a consequent sharp increase a few hours before the earthquake occurred. The disturbances lasted about 3 months and then the intensity level recovered to its orginal level depicted at the beginning of Fig.4. The observations had been carried out for more than ten years and this kind of strange behavior had not been observed previously. They examined various possibilities and finally concluded that the anomaly was likely related to the earthquake.

A third important event was the 1993 Guam earthquake (M 8.0). [57] proposed a new method for detecting earthquake-related ULF emissions with the use of simultaneous reording of orthogonal three geomagnetic components. They demonstrated that the use of the ratio $\left({}^{S_Z}/_{S_H}\right)$, called polarization, is of essential importances in discriminating the seismic emissions from other signals such as

magnetospheric variations. Here $S_Z$ and $S_H$ indicates the spectral intensities of vertical and horizontal components. They found anomalous increase in polarization preceding the earthquake.

# Chapter 3

## Magnetometers

Magnetic field strength is measured using a variety of different technologies. Each technique has unique properties that make it more suitable for particular applications. These applications can range from simple sensing the presence or change in the field to the precise measurements of a magnetic field's scalar and vector properties. A very good and exhaustive fundamental description of both mechanical and electrical means for sensing magnetic fields can be found in Lion [143]. Less detailed but more up-to-date surveys of magnetic sensor technologies can be found in [144][145] . It is not possible to adequately describe all of these technologies in the space available in a Handbook. This chapter concentrates on sensors that are commonly used in magnetic field measuring instruments.

Magnetometers are an instrument to measure the strength or direction of the Earth's magnetic field. The Earth's magnetic field (the magnetosphere Magnetometer is a instrument used to measure the strength or direction) varies both temporally (there is daily variation of around 30nT at mid latitudes and hundreds of nT at the poles) and spatially (from around 20,000 nT near the equator to 80,000 nT near the poles) for various reasons, such as in homogeneity of rocks and the interaction between charged particles from the sun and the magnetosphere. Geomagnetic storms can cause many variations, but on average, the Earth's magnetic field is relatively weak. A simple magnet produces a field hundreds of times stronger. Magnetometers are distinct from metal detectors, which detect metallic objects by detecting their conductivity. Magnetometers can detect only magnetic (ferrous) metals, but can detect such metals at a much larger depth than a metal detector. Magnetometers used in the Earth sciences are called geophysical surveys, a term that also embraces a wide

range of other geophysical techniques including gravity, seismic refraction, seismic reflection, electromagnetic (EM), induced Polarisation (IP), magneto-telluric (MT), Controlled sources magneto-telluric (CSAMT), sub-audio magnetic (SAM), resistivity, self potential (SP) and very low frequency (VLF). Magnetometers can be divided into two basic types:

(1) Scalar magnetometers measures the total strength of the magnetic field to which they are subjected, but not its direction. They include proton pression, Overhauser, and a range of Alkali vapour instruments including Caesium, Helium and Potassium.

(2) Vector magnetometers have the capability to measure the component of the magnetic field in a particular direction, relative to the spatial orientation of the device. Vector magnetometer measures one or more components of the magnetic field electronically. Using three orthogonal magnetometers, both azimuth and dip (inclination) can be measured. By taking the square root of the sum of the squares of the components the total magnetic field strength can be calculated by Pythagoras's theorem. Examples of vector magnetometers are fluxgates, superconducting quantum interference devices (SQUIDs), and the atomic SERF magnetometer. Vector magnetometers are subjected to temperature drift and the dimensional instability of the ferrite cores. They also require levelling to obtain component information, unlike total field (scalar) instruments.

Magnetometers can also be classified as "AC" if they measure fields that vary relatively rapidly in time and "DC" if they measure fields that vary slowly (quasi-static) or are static.AC magnetometers find use in electromagnetic (such as magnetotellurics), and DC magnetometers are used for detecting mineralization and correspond geological structures.

## 3.1 Scalar magnetometers

Scalar magnetometers measure the magnitude of the magnetic field vector by exploiting the atomic and nuclear properties of matter. The two most widely used scalar magnetometers are the proton pression and the optically pumped magnetometer. When operated under the right conditions, these instruments have extremely high resolution and accuracy and are relatively insensitive to orientation. They both have several common operating limitations. The instruments require the magnetic field to be uniform throughout the several common operating limitations. The instruments require the magnetic field to be uniform throughout the sensing element volume. They have a limited magnetic field magnitude measurement range: typically 20 μT to 100 μT. And they have limitations with respect to the orientation of the magnetic field vector relative to the sensor element.

## 3.2 Proton precession Magnetometers

Proton precession magnetometer is based on Zeeman Effect. Proton precession magnetometer uses hydrogen atoms to generate precession signals. Liquids, such as kerosene, are used because they offer very high densities of hydrogen and are not dangerous to handle. A polarizing DC current is passed through a coil wound around a liquid sample (water, kerosene, or similar). This creates an auxiliary magnetic flux density of order of 100 Gauss. Protons in this field are polarized to a stronger net magnetization corresponding to the thermal equilibrium of the stronger magnetic flux density. When the auxiliary flux is terminated quickly, the "polarized" protons presses to re-align them to the normal flux density. The frequency of the precession, $f_0$, relates directly to the magnetic flux density, B, (units of which are teslas,T), according to the following equations:

$$f_0 = \left({}^{\gamma_p}/_{2\pi}\right) B \qquad {}^{\gamma_p}/_{2\pi} = 42.576375 \qquad 3.1$$

The precession signal is present is present from a fraction of a second to up to 2 seconds,

and can be measured using a special counter. Signal quality can also be derived from the signal amplitude and its decay characteristics, which are recording period. Proton precession measurements are necessarily sequential. This means that there is an initial polarization, followed by a frequency measurement after which, the cycle is repeated. This differs from continuous measurements. Where the nuclei are polarized and frequency measurements are made simultaneously. Figure 3.2 is a block diagram of a proton precession magnetometer. The sensor is a container of hydrocarbon rich in free hydrogen nuclei. A solenoid wrapped around the container is used to both polarize the nuclei and detect the

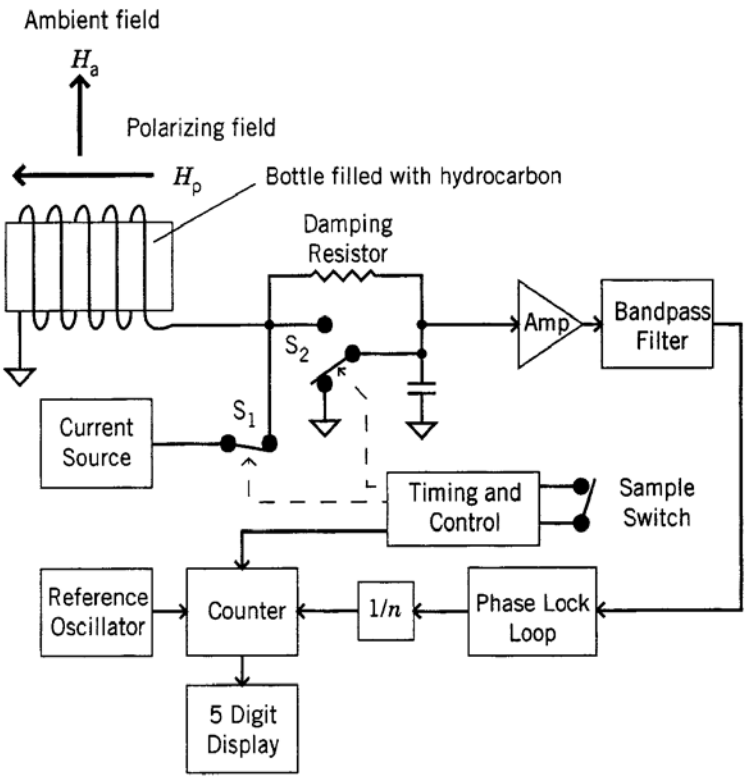


**Figure 3.2:** Typical proton precession magnetometer. A polarizing Field is applied to the hydrocarbon when S1 is closed. The amplifier Input is shorted to prevent switching transients from over driving it after a few seconds, S1 is opened and the coil is connected to the Signal processor to measure the Larmor frequency.

Precession caused by the ambient field. Before the polarizing field is applied, the magnetic moments of the nuclei are randomly oriented, and the net magnetization is zero. Application of the polarizing field (typically 3mT to 10mT) causes the nuclei to presses about the field. The precession axis can be parallel or antiparallel (nuclear magnetic moments pointing in the direction of the field) to the applied field. From a quantum mechanical standpoint, which causes collision between atoms, the fluid will remain unmagnetized. When a collision occurs, the parallel precession-axis nuclei lose energy and switch to the antiparallel state. After a short time, there are more nuclei with magnetic moments pointing in the direction of the field than away from it, and the fluid reaches an equilibrium magnetization $M_0$ .

Once the fluid has reached equilibrium magnetization, the field is removed and the nuclei are allowed to presses about the local ambient field until they become randomized again. This process of excitation relaxation can take as long as several seconds.

## 3.2.1 Signal Conditioning

The block diagram shown in Figure 48.23 is an example of signal conditioning required for a proton precession magnetometer. The coil surrounding the bottle containing the hydrocarbon serves the two purposes. At the beginning of a measurement, the current source is connected to the coil to generate the magnetic field that polarizes the fluid. This field is of the order of 10mT. After a few seconds, the current source is disconnected and the coil, which now has decaying nuclear precession signal at its output, is connected to the input of the amplifier. The signal is amplified, filtered, and then the period of the Larmor frequency is measured, averaged, scaled, and presented to the user in magnetic field units on a digital display. The scale factor of the proton precession magnetometer is based on the gyro magnetic ratio, which is 0.042579 Hz $nT^{-1}$.

High resolution, up to 0.01nT, is achieved by measuring the period of the signal rather than the frequency. The signal frequency can be divided down and used to gate a high-frequency oscillator that is driving a counter. The sampling of the field is controlled manually in many commercially available protons precession magnetometers. Some magnetometers have an internally controlled sample rate. The sample rate and resolution are inversely related to one another. A higher sample rate produces a poorer resolution.

## 3.3 Overhauser Magnetometer

The Overhauser magnetometer, with its unique set of features, represents a pillar of modern magnetometry of the Earth's magnetic field. Its sensitivity matches costlier and less convenient caesium magnetometers, for example. The Overhauser magnetometer also offers superior omnidirectional sensors; no dead zones; no heading errors; or warm-up time prior to surveys; wide temperature range of operation (from -40 to 55 degrees Celsius standard and -55 to 60 degree Celsius optional); rugged and reliable design; and virtually no maintenance during its lifetime. Other advantages include high absolute accuracy, rapid speed of operation (up to 5 readings per second), and exceptionally low power consumption.

Overhauser magnetometers use proton precession signals to measure the magnetic field- but that's where the similarity with the proton precession magnetometer ends.

### 3.3.1 Operating Principle

The Overhauser effect takes advantage of quantum physics effect that applies to the hydrogen atom. This effect occurs when a special liquid (containing free, unpaired electrons) is combined with hydrogen atoms and then exposed to secondary polarization from a radio frequency (RF) magnetic field (i.e. generated from a RF source).RF magnetic fields are ideal for use in magnetic devices because they are "tr-

ansparent" to the Earth's "DC" magnetic field and the RF frequency is well out of the bandwidth of the precession signal (i.e. they do not contribute noise to the measuring systems).The unbound electrons in the special liquid transfer their excited state (i.e. energy) to the hydrogen nuclei (i.e. protons). This transfer of energy alters the spin state populations of the protons and polarizes the liquid- just like a proton precession magnetometer- but with much less power and to much greater extent. The Proportionality of the precession frequency and magnetic flux density is perfectly linear, independent of temperature and only slightly affected by shielding effects of hydrogen orbital electrons. The constant of proportionality,$\gamma_p$, is Known to a high degree of accuracy and is identical to the proton precession gyro magnetic constant. The advantage of Overhauser magnetometer over other magnetometers is that they have greater sensitivity even in the lowest of Earth's fields. Their sensitivity that virtually matches cesium sensitivity. This is the only quantum magnetometer that offers continuous or sequential operations. With Overhauser magnetometers, it is possible to measure continuously or sequentially due to the use of an RF polarization field. The RF field is transparent to the use measurement of magnetic field and can therefore, be enabled at all times. The sampling rate is higher (as high as 10 Hz possible). Overhauser magnetometers are significantly more efficient than any other quantum magnetometer due to low power required for RF signal generation. Power consumption can be optimized to as low as 1W for continuous operation. Omnidirectional sensors. No dead zones, virtually no heading errors and no warm up time. There are also other advantages related to the manufacturing process (which are of less interest to users), such as relative simplicity, reliability of design, relatively low manufacturing cost relative to sensitivity, weight and power consumption benefits.

## 3.4. The Optically Pumped Magnetometers

As explained earlier, the optically pumped magnetometer is based on the Zeeman Effect. This effect is most pronounced in alkaline vapours (rubidium, lithium, caesium, sodium, and potassium). Figure 3.4 is the hyperfine spectral structure for the valence electrons of rubidium (Rb) 85, which is commonly used in these types of magnetometers. The energy-related frequency interval between these hyperfine lines is proportional to the applied field. The magnetic quantum number m is related to the angular momentum number and specifies the possible component magnitude of the magnetic moment along the applied field. The optically pumped magnetometer takes advantage of this characteristic. Transitions occur between levels of different m values and obey the rule that the change in m can only have the values 0, 1, and -1. Table 3.4 lists the relationship between the polarization of the light stimulating the

**Table 3.4:** The Allowable Change in m When Jumping One Energy Level to Another Depends on Polarization of the Light Causing the Transition

| Polarization | m |
|---|---|
| Left Circular | -1 |
| Parallel | 0 |
| Right Circular | 1 |

transition and When not optically excited, the energy states of the valance electrons will be distributed according to the Boltzmann statistics and will be in the state of equilibrium. If the electrons are excited with circularly polarized light at the D1 frequency (794.8 nm wavelength), they will absorb photons and transition from the $^2S_{1/2}$ state to the $^2P_{1/2}$ state according to transition rules. The excited electrons will then fall back in the random fashion to the lower states, being distributed with an equal probability among all the m states. But the rule states that the change in m can only be 1 or -1 for polarized light. If one uses right circularly polarized light, then the

change in m can only be 1, and the electrons in the m=3 level of the $^2S_{1/2}$ state cannot transition since there is no m=4 level at the $^2P_{1/2}$ state. Therefore, these electrons remain in the m=3 state. All other electrons transition to the higher state and then fall back to the lower state with equal probability of arriving at any of the m levels, including m=3 level, and no more transition to the higher state can take place. Pumping stops. When pumping begins, the vapour is opaque. As time goes on, less electrons are available for absorbing photons, and the vapour becomes more transparent until, finally, pumping action stops and the vapour is completely

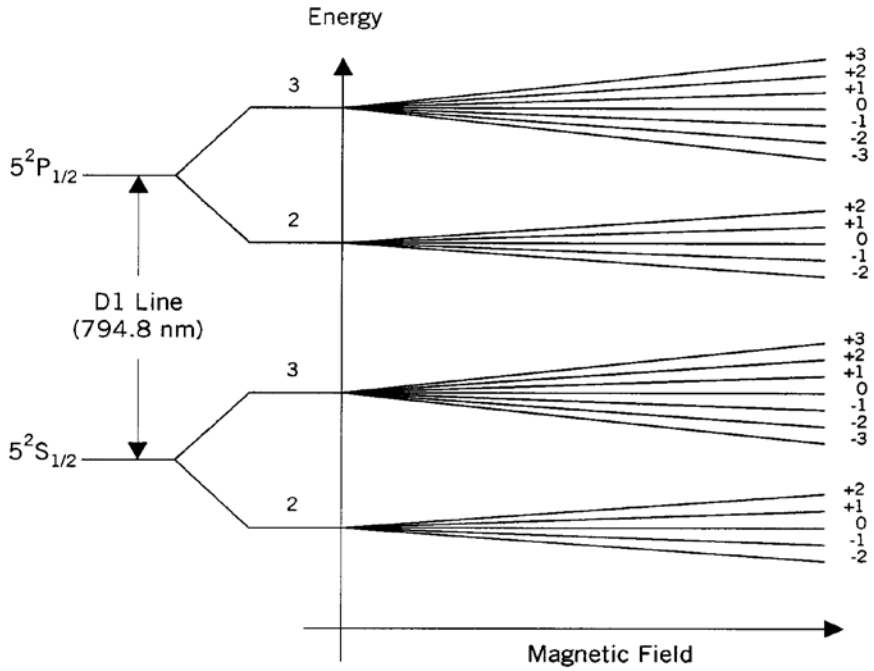


**Figure 3.4:** Rb-85 energy diagrams. When a magnetic field is applied, the energy levels split into Zeeman sublevels that diverge as the field Increases. Quantum mechanical factor determines the number of sub-Levels at each primary energy level.

Transparent. If a small RF magnetic field at the Larmor frequency is applied at right angles to the magnetic field being measured, the electrons in the m=3 state will be

depumped to the other m levels, making them available for further pumping. The optically pumped magnetometer exploits this situation in a positive feedback arrangement to produce an oscillator at the Larmor frequency. The scale factors for optically pumped magnetometers are significantly higher than for the proton precession magnetometers.

## 3.4.1 Signal Conditioning

Descriptions of several optically pumped magnetometers and their operating principles can be found in[146][147][148]. There are a number of different signal conditioning arrangements that can be used to derive a useful readout of the measured fields. Two of the more common methods are described in[148] and are shown in figure 3.4

In the served type shown in figure 3.4(a), the magnetic field being measured and the RF oscillator is modulated with a low- frequency oscillator. This causes the RF frequency to sweep through the Larmor frequency. If the seeped RF oscillator is not centred about the Larmor frequency, the photo cell output signal will contain a fundamental component of the RF modulation frequency. The phase of the signal relative to the modulator oscillator determines whether the central RF frequency is above or below the Larmor frequency. The photocell output is phase-detected to produce an error voltage that is used to drive the RF frequency towards the Larmor frequency. The RF frequency can be measured to determine the magnetic field. If a linear voltage controlled oscillator is used as the RF oscillator, its controlled voltage can also be used as an output since it is a measure of the Larmor frequency. The auto-oscillating type shown in figure 3.4(b) is based on the transmission of a polarized beam that is at right angles to the field being measured. The intensity of this cross-beam will be modulated at the Larmor frequency. The photocell signal will be shifted

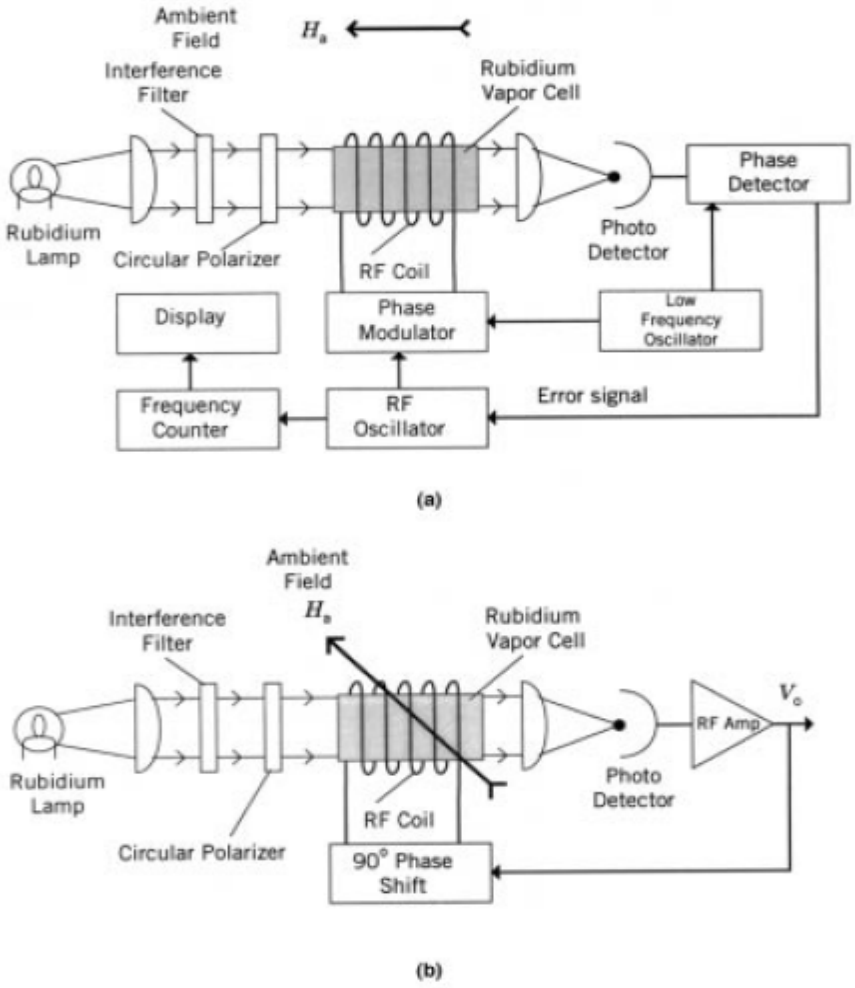


**Figure3.4:** Two examples of optically pumped scalar magnetometers the served magnetometer: (a) slightly modulates the RF field at a low Frequency, causing the vapour transmissivity to modulate. A phase Detector provides an error signal that is used to lock the RF oscillator to the Larmor frequency. (b) A self-oscillating magnetometer: the Transmissivity of the vapour, at right angles to the applied field, is made to oscillate at the Larmor frequency by phase –shifting the Light modulation and feeding it back to the RF field generator. (Adapted from Hartmann, 1972.).

by $90^0$ relative to the RF field. By amplifying the photocell signal, shifted by $90^0$and feeding it back to drive the RF field coil, an oscillator is created at the Larmor frequency. In practice, only one light source is used, and the field being measured is set at an angle of $45^0$

## 3.5 Low Field Vector Magnetometers

Vector magnetometers have the capability to measure the component of the magnetic field in a particular direction, relative to the spatial orientation of the device. Vector magnetometer measures one or more components of the magnetic field electronically. Using three orthogonal magnetometers, both azimuth and dip (inclination) can be measured. By taking the square root of the sum of the squares of the components the total magnetic field strength can be calculated by Pythagoras's theorem. Examples of vector magnetometers are fluxgates, superconducting quantum interference devices (SQUIDs), and the atomic SERF magnetometer.

## 3.6 The Fluxgate Magnetometer

The fluxgate magnetometer has been and is workhorse of magnetic field strength instruments both on earth and space. It is rugged, reliable, physically small, and requires very little power to operate. These characteristics, along with its ability to measure the vector components of magnetic fields over a 0.1 nT to 1 mT range from dc to several kHz, make it a versatile instrument. Geologists use them for exploration and geophysicists use them to study the geomagnetic fields.

### 3.6.1 The Fluxgate

The heart of the fluxgate magnetometer is fluxgate. It is the transducer that converts a magnetic field into electric voltage. There are many different fluxgate configurations. Two of the more popular ones are shown in figure3.6.1. A very comprehensive expla-

nation of the fluxgate principle and the different fluxgate configurations is given in[149]. The ring core fluxgate is constructed from a thin ribbon of easily saturable ferromagnetic material, such as 4-79 perm alloy wrapped around a bobbin to Form a ring core or torrid. As shown in figure 3.6.2, an alternate current is applied through a coil that is wound about the toriod. This creates a magnetic field that circulates around the magnetic core. This magnetic field causes the flux in the ferrous material of periodically saturate first clockwise and then counter clockwise. A pick-up (signal) winding is wrapped around the outside of the toriod. While the ferrous material is between saturation extremes, it maintains an average permeability much greater than

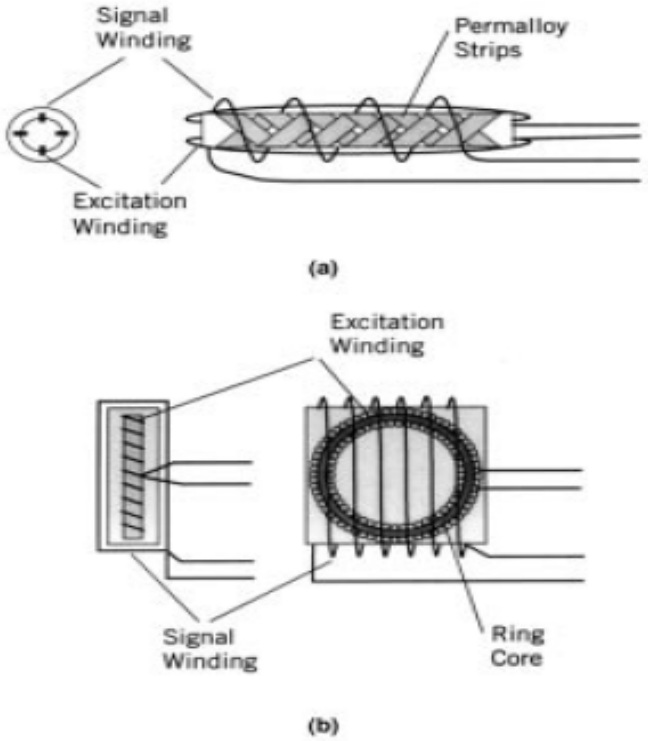


**Figure 3.6.1:** in Schonstedt (a) and ring core (b) fluxgate sensors, the excitation field is at right angles to the signal winding axis. This configuration minimizes coupling between the excitation field and the signal winding.

that of air. If there is no component of magnetic field along the axis of signal winding, the flux change seen by the winding is zero. If, on the other hand, a field component is present along the signal winding axis, then each time the ferrous material goes from one saturation extreme to the other, the flux within the core will change from a low level to the high level. According to faraday's law, a changing flux will produce a voltage at the terminals of the signal winding that is proportional to the rate of change of flux. For dc and low-frequency magnetic fields, the signal winding voltage is:

$$e(t) = nA\frac{d(\mu_0\mu_e H)}{dt} = nA\mu_0\frac{d\mu_{e(t)}}{dt} \qquad 3.2$$

Where H= Component of the magnetic field being measured, n= Number of turns on the signal winding, A= Cross-sectional area of the signal winding, $\mu_{e(t)=}$ Effective relative permeability of the core.

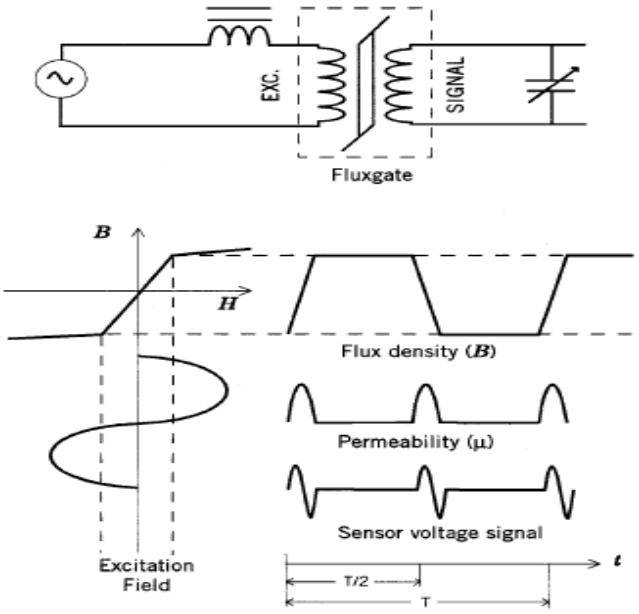


**Figure 3.6.2**: The excitation field of a fluxgate magnetometer alternately drives the core into positive or negative saturation, causing the core's effective permeability to switch between 1 and a large value twice each cycle.

As the core permeability alternates from a low value to a high value, it produces a voltage pulse at the signal winding output that has amplitude proportional to the magnitude of the external magnetic field and a phase indicating the direction of the field. The frequency of the signal is twice the excitation frequency since the saturation-to-saturation transition occurs twice each excitation period. The fluxgate effective permeability and the signal characteristics as they relate to excitation field level, excitation waveform and winding geometry is comprehensively discussed in [149] [150][151][152].

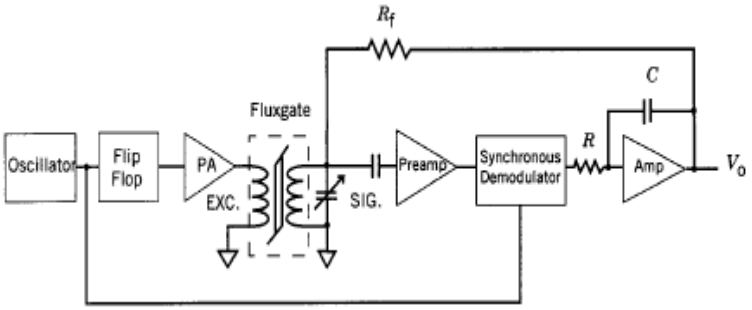


**Figure 3.6.3:** Typical circuit configurations for a field feedback fluxgate magnetometer. The sensor output is an ac amplified, synchronously demodulated, and filtered. A magnetic field that nulls the ambient field that nulls the ambient field at the sensor is produced by connecting the resistor $R_f$ between the output and the signal winding.

## 3.6.2 Signal Conditioning

The signal from the fluxgate is an amplitude suppressed carrier signal that is synchronous with the second harmonic of the excitation signal. In a simple low-power magnetometer, this signal is converted to the base band using a synchronous demodulator, filtered, and presented as the final output. Example circuit are given in[150][151] . The accuracy of magnetometers that use this open-loop architecture is

Limited by the linearity of the core's magnetization curve and is about 5% for Earth's field (60μT) applications.More precise and stable magnetometers use Magnetic field feedback rather than the open-loop structure described above. A simplified schematic of a typical second harmonic feedback fluxgate magnetometer is shown in figure 3.6.3. The circuitry to the left of the fluxgate is called the excitation circuit. It consists of an oscillator tuned to twice the excitation frequency, a flip-flop that divides the oscillator frequency by two and a power amplifier driven by the flip-flop and, in turn, provides the excitation current to the excitation winding.

The circuitry to the right of the fluxgate is called the signal channel circuit. It amplifies the output from the fluxgate winding, synchronously demodulates the ac signal using the oscillator signal as a reference, integrates and amplifies the base band output, and then feed-back the output through a resistor to the signal winding. The feed-back signal produces a magnetic field inside the sensor that opposes the external field. This keeps the field inside the sensor near zero and in a linear portion of the magnetization curve of the ferromagnetic core. The flow diagram for the magnetometer is given in figure 3.6.4. The external field $H_a$ is opposed by the feedback field $H_f$ and the difference is converted into a voltage signal ($K_s$ represents the transfer function from current to field). The overall transfer function for the magnetometer is:

$$\frac{V_0}{H_a} = \frac{AK_s}{1+\frac{K_c A K_s}{R_f}} \qquad 3.3$$

The amplifier gain is normally very high such that the second term in the denominator is much large than one, and Equation 48.29 reduces to

$$\frac{V_0}{H_a} = \frac{R_f}{K_c} \qquad 3.4$$

Under these circumstances, the transfer function becomes almost completely determined by the ratio of $R_f$ (the feedback resistor) $K_c$ (the current-to-field coil

constant of the sensor winding). Both of these constants can be very well controlled. The consequence of this circuit topology is a highly stable and accurate magnetometer that is insensitive to circuit component variations with temperature or time. An accuracy of 1% over a temperature range of $-80^0$C to $80^0$C is easily achievable. Accuracy and stability can be improved using a current feedback circuit, like the one described in[152] , that compensates for the resistance of the signal winding or by using a separate feedback winding and a high-quality voltage-to-current converter instead of a simple feedback resistor.

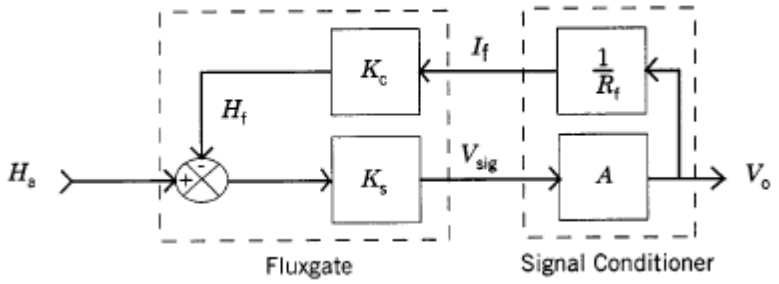


**Figure 3.6.4:** Typical circuit configuration for a field feedback fluxgate magnetometer. The sensor output is an ac amplified, synchronously demodulated, and filtered. A magnetic field that nulls the ambient field at the sensor is produced by connecting the resistor$R_f$ between the output and the signal winding.

# 3.7 The SQUID Magnetometer

Brian D. Josephson in 1962, while a graduate student at Cambridge University, predicted that superconducting current could flow between two superconductors that are separated by a thin insulating layer. The magnitude of the superconductor (critical) current through this "Josephson junction" is affected by the presence of a magnetic field and forms the basis for the SQUID magnetometer.

Figure3.7 illustrates the general structure of a Josephson junction and the voltage current (V-I) relationship. Two superconductors (e.g., niobium) are separated by a

thin insulating layer (e.g., aluminium oxide). The thickness of this layer is typically 1 nm. When the temperature of the junction is reduced to below 4.2K (-269), a superconductor current will flow in the junction with 0V across the junction. The magnitude of this current, called the critical current, called the critical current$I_c$, is a periodic function of the magnetic flux present in the junction. Its maximum magnitude occurs for flux values equal to n$\varphi_0$, where $\varphi_0$, is one flux quantum( 2fw), and it maximum magnitude occurs for the flux values equal to$\left(n+\frac{1}{2}\right)\varphi_0$. The period is one flux quantum. This phenomenon is called the “dc s

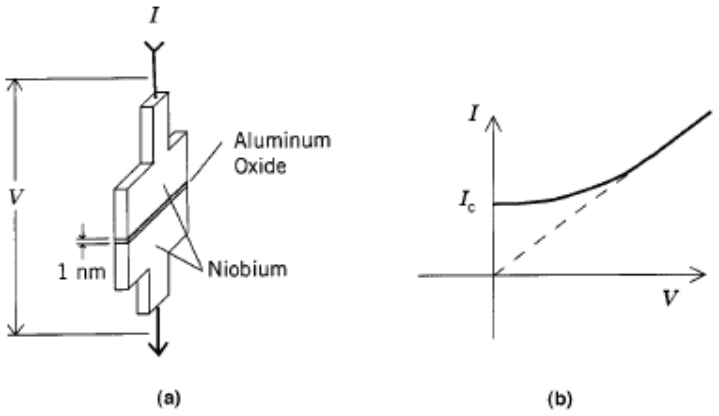


**Figure 3.7:** The Josephson junction in (a) consists of a superconductor such as niobium separated by a thin insulation layer. The voltage (V) $v_s$ current (I) curve in (b) shows that a superconducting current flows through the junction with zero volts across the junction

Magnetometers based on the Superconducting Quantum Interference Device (SQUID) are currently the most sensitive instruments available for measuring magnetic field strength. SQUID magnetometers measure the change in the magnetic field for some arbitrary field level; they do not intrinsically measure the absolute value of the field. SQUID magnetometers and gradiometers (measure spatial variation in the magnetic field) have the high sensitivities needed to measure the weak magnetic fields generated by the body[153]. Other application area includes paleo-

magnetics (measuring remnant magnetism in rocks) and magnetotellurics (Earths resistivity measurements). Description of these applications as well as the general theory of SQUIDs can be found in[154]. Clark[155], one of the pioneers in SQUID magnetometers, provides a good contemporary overview of SQUID technology and applications. A dc SQUID magnetometer uses two Josephson junctions in the two legs of a toriod as shown in Figure 48.12(a). The toriod is biased with a constant current that exceeds the maximum critical current of the junction. When the flux through the toriod is an integral multiple of$\varphi_0$, the voltage across the junction is determined by the interaction of $I_b$ and the curve (point A). As the flux increases, the critical current decreases. The I-V curve and thus the interaction point move to the right (the junction voltage increases). The critical current reaches a minimum when the flux has increased by n$\varphi_0$ and the junction voltage is at its maximum (point B). As the flux continues to increase, the critical current increases back towards its maximum value and the junction voltage decreases. Thus, the period of the flux cycle is $\varphi_0$.

## 3.7.1 Signal Conditioning

Figure 3.7 is a block diagram of one implementation of a dc SQUID magnetometer that can be used for wide dynamic range field measurements. A large superconducting loop, which is exposed to the magnetic field being measured, is connected to a multiturn signal winding that is magnetically coupled directly to the SQUID. At cryogenic temperatures, the loop and signal winding effectively form a dc induction coil. External flux applied to the coil will generate a current in the loop that keeps the net flux that is applied to the SQUID. The SQUID is magnetically biased at an optimal sensitivity point. A small ac magnetic field at 100 kHz to 500 kHz is superimposed on the bais field. The output of the SQUID is a suppressed carrier amplitude modulated signal where the amplitude indicates the change in magnetic field from the bais point, and the phase indicates the polarity of the change. The out-

put signal is amplified and then synchronously demodulated down to the base band. The resulting dc signal is amplified and fed back through a resistor to a coil coupled to the SQUID. The current through the coil generates a magnetic field at the SQUID that opposes the applied field. This keeps the SQUID operating point very near the bais point. The scale Factor of the magnetometer depends on the feedback resistor and the coil constant of the feedback winding in the same manner that it does for a field feedback fluxgate magnetometer. The pick-up loop, signal coil, SQUID, feedback coil and feedback resistor are kept in a cryogenic temperature chamber and, except for the pick-up coil, are magnetically shielded. The rest of the circuit is operated at room temperature.

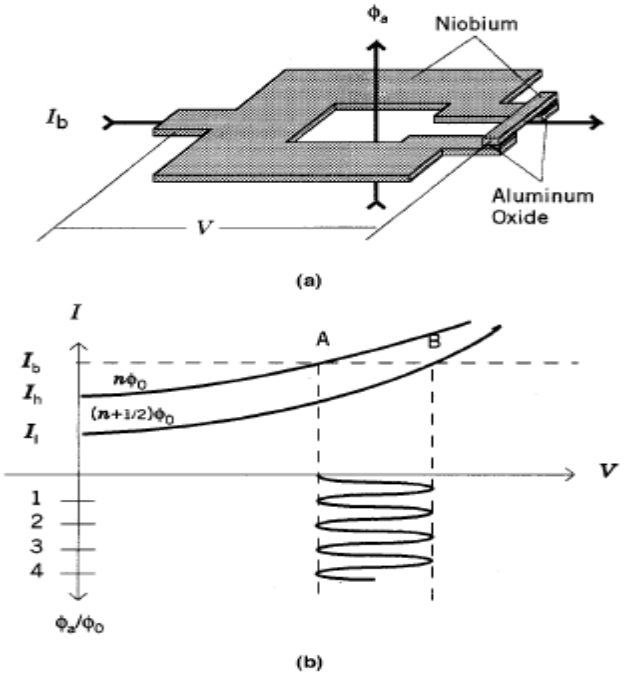


**Figure 3.7:** Use of a dc SQUID to measure magnetic flux. The dc SQUID in (a) consists of a superconductor loop and two Josephson junctions with a bias current that is greater than the maximum critical current$I_h$. The V-I curve in (b) illustrates how the voltage across the SQUID oscillates with a period equal to one flux quantum $\varphi_{0.}$

## 3.8 The induction Coil Magnetometer

The induction or search coil, which is one of the simplest magnetic field sensing devices, is based on Faraday's law. This law states that if wire is subjected to a changing magnetic flux, through the area enclosed by the loop, then a voltage will be induced in the loop that is proportional to the rate of change of flux:

$$e(t) = -\frac{d\varphi}{dt} \qquad 3.5$$

Since magnetic induction B is flux density, and then a loop with cross-sectional area A will have a terminal voltage:

$$e(t) = -\frac{d(B.A)}{dt} \qquad 3.6$$

Equation 3.5 states that a temporal change in B or the mechanical orientation of A relative to B will produce a terminal voltage. If the coil remains fixed with respect to B, then it is possible to measure a static field. The relationship described by Equation 3.5 is exploited in many magnetic field measuring instruments [143]. Figure 3.8 shows the two most common induction coil configurations for measuring field strength: the air core loop antenna and the rod antenna. The operating principle is same for both configurations. Substituting $\varphi$ For B in equation 3.6 and, assume the loop is stationary with respect to the field vector, the terminal voltage becomes:

$$e(t) = -\mu_0 \mu_e nA \frac{dH(t)}{dt} \qquad 3.7$$

Where n is the number of turns in the coil, and  is the effective relative permeability of the core. The core of the rod antenna is normally constructed of magnetically "soft" material so one can assume the flux density in the core is induced by an external magnetic field and, therefore, the substitution above is valid. With an air (no) core, the effective relative permeability is one. The effective permeability of an induction coil that contains a core is usually much greater than one and is strongly

dependent on the shape of the core and, to some extent, on the configuration of the winding.

Taking the Laplace transform of Equation 3.7 and dividing both sides by H, one obtains the following transfer function T(s) for an induction coil antenna.

$$T(s) = -\mu_0 \mu_e nAs = -Ks(VmA^{-1}) \qquad 3.8$$

Where E(s) = T(s) H(s), E(s) and H(s) are Laplace transforms of e(t) and H(t), and s is the Laplace transform operator. Inspection of Equation 3.8 reveals that the magnitude of the coil voltage is proportional to both the magnitude and frequency of the coil voltage is proportional to both the magnitude and frequency of the magnetic field being measured. The constant or sensitivity of the loop antenna is:

$$K = \mu_0 \mu_e A(VsmA^{-1}) \qquad 3.9$$

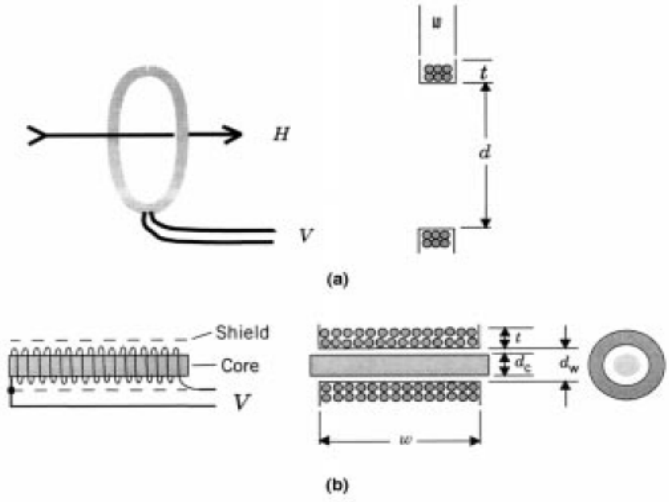


**Figure 3.8:** Induction or search coil sensor consists of a loop of wire (or a solenoid), which may or may not surround a ferromagnetic core. (a) Air core loop antenna; (b) solenoid induction coil antenna with ferromagnetic core.

**Figure 3.9:** is the equivalent circuit for an induction coil antenna. The actual voltage measured at the terminals of the loop is modified by the inductance L, resistances R, and the distributed stray and shield capacitances represented by the lumped capacitor C. These circuit parameters depend on the geometry of the core, coil, and winding. The electrostatic shield made of non magnetic material shown in figure 3.8 is an important element in the design of an induction coil. It prevents coupling of the electric fields into the coil, thereby assuring that the signal seen at the coil terminals is only due to a magnetic field. The shield should not be placed too close to the winding since it contributes to coil capacitance and noise.

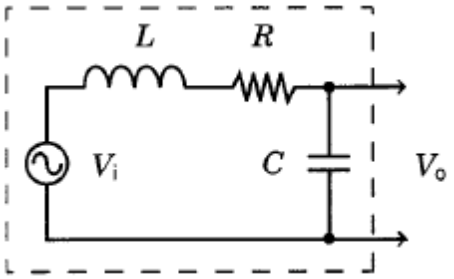


**Figure 3.9:** The induction coil equivalent circuit is a frequency-dependent voltage source in series with an inductor, resistor, and lumped capacitor.

# 3.9 Torsion magnetometer

The classical magnetometers are based on the observation of a magnetic in a changing magnetic field. The magnetic is suspended by a thin fibre. The torque of the magnetic field on the suspended magnetic is compensated by the torque of the suspension fibre. The basic equation for torque T, in the static case when the magnetic field is not changing, is

$$m \times B = T \qquad 3.10$$

Where m is the vector magnetic moment, B is the vector describing the magnetic

field. For a horizontal field h the formula of equilibrium is given by the formula as

$$mH\sin \propto = c\varphi \qquad 3.11$$

where m stands for the magnetic moment of the magnet, cis the torsion constant of the fibre, $\propto$ is the angle between the magnetic meridian and the magnetic axies of the magnet, $\varphi$ is the angle of twisting of the fiber,and His the horizontal component of the magnetic field.

## 3.10 Quartz and its properties

The quartz crystal or resonator operates due to the piezoelectric effect. The piezoelectric effect of quartz allows it to produce an electrical charge on its surface when the same surface(s) are distorted or subjected to pressure. This distortion allows the crystal to vibrate at a particular resonant frequency. Conversely, the application of an alternating voltage produces the same type of mechanical vibration.

Quartz is one of several forms of silicon dioxide ($SiO_2$) that is found in nature; most of the quartz used for crystal fabrication today is of the “cultured” or synthetic variety. Cultured quartz is produced by placing small seeds of quartz mixed with an alkaline solution in an autoclave. This mixture is subjected to high heat ($> 400^0$C) and high pressure (30,000 psi). This causes the quartz to dissolve and reform as thin slices of quartz. This process takes approximately 30-45 days. Quartz is ideal for use as a frequency determining device because of its predictable thermal, mechanical, and electrical characteristic. The quartz crystal is one of the few devices that can provide a high-Q (quality factor) that is needed for precise frequency control in oscillators as a timing standard.

## 3.10.1 vibrational Modes and Orientation Angle

There are many different modes for crystals vibrational modes for crystals as shown in Figure 3.9.1. The frequency versus temperature characteristics of quartz crystal are primarily determined by the orientation angle at which the quartz wafers are cut from a given bar of quartz.

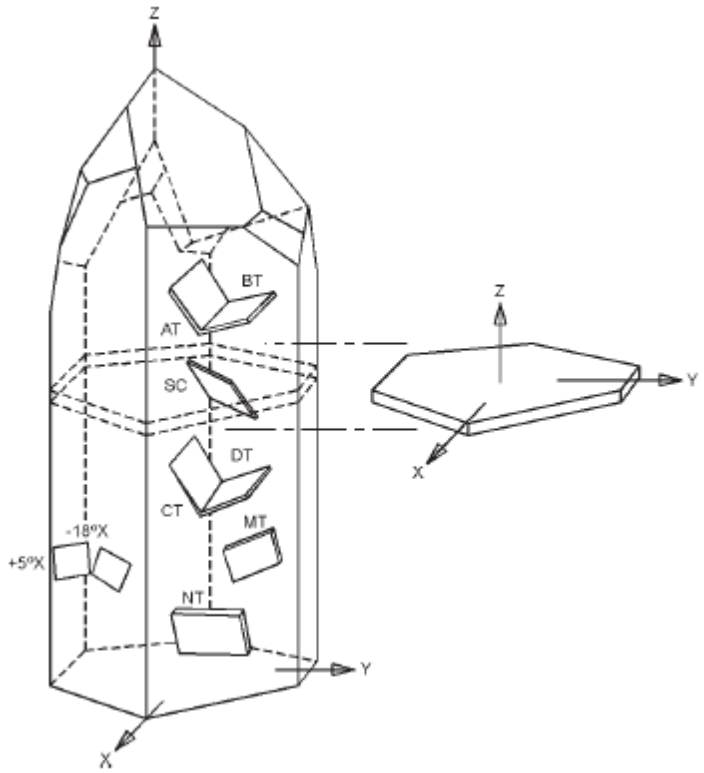


**Figure 3.9.1**

These properties are dependent on the reference directions w there are three axes in quartz, the X, the Y and the Z. An ideal crystal would consist of a hexagonal prism with six facets at each end. See Figure 3.9.1. A cross section taken from that prism would look like the depiction in figure 2ithin the crystals. These directions are referred to as “axes”. The Z-axis is known as the “optical” axis and repeats its physic-

cal properties every $120^0$as the crystal is rotated about the Z-axis. The X-axis is parallel to a line bisecting the angles between adjacent prism faces. This axis is called the “electrical” axis. Electrical polarization occurs in this direction when mechanical pressure is applied. An XT-cut crystal is produced from a slab of quartz cut from that portion of the quartz bar that is perpendicular to the X-axis. Yhe XT-cut crystal if often referred to as a “tuning fork” crystal and is used extensively for 32.768 kHz crystals such as the M-tron MMCC-1, MMCC-2, and SX 1555. The frequency vs. Temperature for the XT-cut crystal is shown in fig 3.9.2. The Y-axis, which is also known as the “mechanical axis”, runs at right angles through the face of the prism, and at right angles to the X-axis. Most Y-axis crystals vibrate in their “sheer modes”, face shear for low frequency CT and DT cut crystals, and the thickness shear for higher frequency AT and BT cut crystals. The AT cut is the most popular of the Y-axis group because of its excellent frequency vs. Temperature characteristics. The AT cut is produced by cutting the quartz bar at an angle of approximately $35^015'$ from the Z-axis.

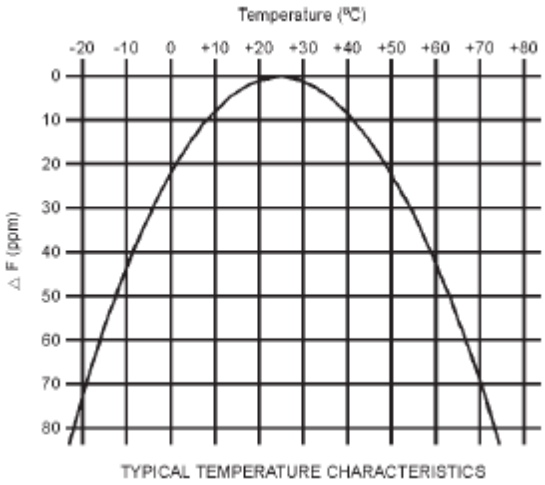


Figure 3.9.2

The crystal resonator is usually a round disc. The thickness (d) of the disc is related to the fundamental mode frequency (f) by the equation:

$$f(\text{kHz} = \frac{N}{d(\text{mm})} \qquad 3.12$$

Where N=1660 kHz ×mm

The crystal has electrodes deposited on both sides. These electrodes are made of a low resistance metal such as silver, gold and aluminium. The electrode structure allows for an electrical voltage to be applied to the crystal in order to produce mechanical vibration. The electrode also provides a means of attaching the crystal to the mounting structure of the crystal base. Because the frequency of the crystal is related to its thickness, there is a limitation in the manufacturing of high frequency fundamental crystals. The higher the frequency, the thinner the crystal blanks. Crystals will also exhibit unwanted or spurious modes when oscillating at the design frequency. These unwanted modes are influenced by the crystal surface finish, diameter and thickness dimensions, and mounting technique. These spurious modes are expressed in terms of equivalent series resistance referenced to the design mode of the crystal, or in terms of energy level in dB referenced to the carrier frequency.

## 3.10.2 Crystal Equivalent Circuit, Motional Parameters, and Quality Factor

The quartz crystal can be represented electrically by the circuit shown in fig 6. The motional inductance ($L_m$), motional capacitance ($C_m$), and series resistance (R) form a series resonant CIR order of 4 to 7 pF. All these motional parameters can be measured using a crystal impedance (CI) .Normally the actual values for these motional parameters are a function of the design frequency. In applications requiring control of spurious responses or where the crystal needs to be “pulled” in frequency, the designer may need to specify the desired motional parameters.

The series resonant frequency (Hz) of the crystal is represented by the formula:

$$FS = \frac{1}{2\pi\sqrt{L_m C_m}} \qquad 3.13$$

Where $L_m$ is in Henries and $C_m$ in Farads.

The "Q" of a crystal is the quality factor of the motional parameters at resonance. The maximum stability of a crystal is directly related to the "Q" of the crystal. The higher the "Q" the smaller the bandwidth and the steeper the reactance curve. The "Q" can be expressed as:

$$Q = \frac{1}{2\pi F_s R C_m} = \frac{2\pi F_s L_m}{R} \qquad 3.14$$

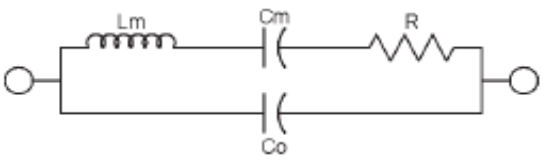


**Figure 3.9.2**

## 3.10.3 Series and Parallel Resonance

When a crystal is operating at series resonance ($f_s$), see figure 7, it appears resistive in the oscillator circuit. The impedance of the crystal is near zero at resonance. No load capacitance needs to be specified for crystals intended for use in a series resonant oscillator circuit. Higher overtone (5th, 7th, and 9th) crystals will be specified as series resonant type .When a crystal is operating at parallel or anti resonance ($f_a$) see

Figure7, it appears inductive in the oscillator circuit. The crystal's impedance is highest at this anti-resonance point. Under this condition the crystal is sensitive to changes in circuit reactance values. For crystal operating in a parallel resonant oscillator the load capacity of the crystal should always be specified in order to insure proper frequency control and operation.

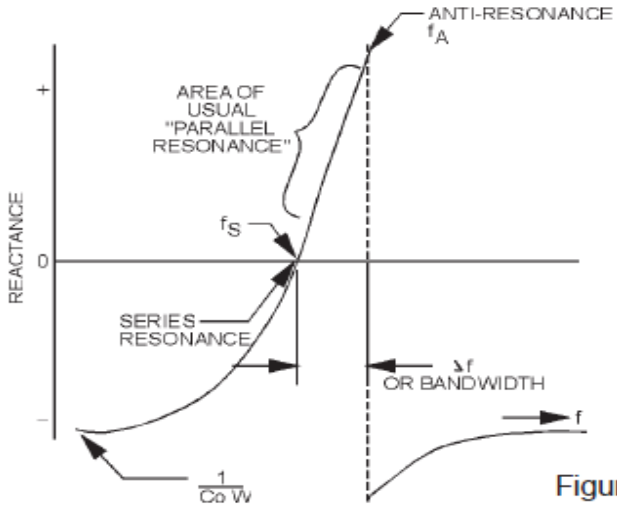

Figure 7

## 3.10.4 Stability Tolerance vs. Frequency Tolerance

The stability tolerance is the maximum allowable deviation from the crystal frequency over a defined operating temperature range. The stability tolerance is usually stated in parts per million (ppm) and is referenced to the frequency of the crystal at room temperature ($+25^0$C). The frequency tolerance of the crystal is the maximum allowable deviation from nominal frequency at a specified temperature, usually $+25^0$C. The stability tolerance of a crystal needs to be specified along with the operating temperature range.

# Chapter 4

## Recording of Magnetic Field Variations

Magnetic variometers are magnetometers which continuously measure and record the magnetic field variations. Three components of the field are usually recorded. For special purposes, like functioning as a base station for prospecting, one component, usually F in this case, might be enough. In observatory use three components are recorded, and often F with proton magnetometer as an additional, absolute verification. The most commonly used variometers at modern magnetic observatories are three-component fluxgate magnetometers combined with microprocessor-based digital data collection.

The data are samples of the magnitude of the field components variations. The primary samples are usually taken at very short intervals, several times per second. Applying digital filtering techniques, one-minute or more dense values are produced and stored. If magnetic pulsation have to be recorded using the same original data, much denser component values have to be stored and a higher resolution has to be used. As a rule, the sample represent only the varying part of the field, having a range of $\pm$4000 nT or so, and a base value has to be added to the recorded one for getting the final value of the component.

## 4.1 Installation of the Station

The sensor of the variometer usually has two perpendicular levels. If not, separate levels have to be used. Their reading corresponding to the correct vertical position of the Z-sensor should be kept in mind from the calibration at the magnetic standard observatory. This makes it easy to install the sensor at its final place, so that the vertical intensity is measured correctly. If the sensor head can be turned around its vertical axis, the verticality can be checked by adjusting the sensor until the Z-sensor shows the same value in all positions. If the components H and D will be recorded, then the installation is easy: just

turn the sensor until the D-component shows zero value (in undisturbed field). But after a few years, due to the secular variation, the orientation will no longer be in the H-D direction, and the sensor will have to be turned or one will have to introduce small corrections to the components.

The installation to measure the north and east components, X and Y, can be done simply by turning the sensor until the Y-component shows the value of the known Y at the pillar. Another method is to use the north-south or east-west lines marked on the sensor at the standard observatory in the calibration process, and to install the sensor at the pillar utilizing the N-S or E-W lines drawn on the pillar.

Making use of modern microprocessor technology it is possible to install the sensor in arbitrary positions and calculate the desire components. The orientations can be calculated from absolute measurements, provided full components are recorded.

## 4.2 Analogue Recording

The classical, traditional method of recording the variations of three components of the earth's magnetic field is photographic. The light from one or more lamps is reflected from the mirrors of magnetometers (one fixed mirror for the base-line and one mirror fixed to the moving magnet) to photo paper which is wrapped on a drum.

The analogue photographic recordings have been in use for more than hundred years and are still in wide use. They are reliable and practically no service is needed besides the change of lamp once a year or so on. If a flashing lamp is used, the lamp seems to last many years. Once in, say, five years some service is needed to the clock which drives the photo paper drum. The analogue curve on the photo paper is produced by a light beam without any friction in the system, which is an advantage compared to the ink recorders. One shortcoming in the photographic recording is the disappearance of the curve during rapid change of the field, or, if the rapid changes are made visible, the curve during quite times is too thick. This shortcoming can be

avoided by letting the lamp flash every ten seconds and not letting it to be on all the time. By making the lamp stay on for a longer time every ten minutes and even longer at a full hour, the trace will have the time marks. For the ten-second flashes the lamp may be on for one second. Two separate recording systems are recommended for magnetic observatories. The old photographic system may be kept as a supplementary one if funds and space permit. Monitoring the magnetic field in real time is highly recommended, because the observatories should be prepared to answer questions on the behaviour of the magnetic field in almost real time. Visualizing digital data at the computer screen as graphs of the components of the magnetic field is naturally one good way to monitor the field. To keep a chart recorder running for the monitoring is also a simple and economic way.

## 4.3 Digital Recording

During recent years, several institutes have made their own digital loggers for the collection of geomagnetic data in digital form. Some of these have even be made commercial. The rapid development in processors, personal computers (PC's), lap-top computers and hard discs and even optical discs have opened an enormous variety of possibilities to use commercially available, not too expensive equipment for the data collection. Suitable hardware is easy to obtain in most places, and the main problem lies in programming the processor or the computer.

When applied to geomagnetic work, the commercial PC's have two problems. One is that most of them need power from normal mains, 110 or 240 V ac. As stressed several times, the magnetic recording should not have gapes, and the mains sometimes have interruptions.

The original signals from variometers are usually in volts, which mean that analogue to digital (A/D) conversion has to be made before the data can be treated and stored. To be able to record variations of the order of ±4000 nT with a resolution

of 0.1 nT, which are realistic figures, that means the sign and 16 bits. Fast, stable and reliable A/D converters for even more bits are available. But because the converters are fast enough, it is possible to use the same converters for all the three components.

## 4.4 Analysis Methods of ULF Magnetic field variations

Not only installing highly sensitive ULF sensors as described in the previous chapter, but also carrying out different sophisticated signal processing's highly required to detect and identify weak seismogenic ULF emissions even in the noisy electromagnetic environment. Several useful signal processing's have already been developed, some of which will be described below.

### 4.4.1 Cumulative Probability Plots

A few serious problems that must be overcome in the study of EQ signatures in the ULF data are the complexity of the background from other natural and man-made sources and the low probability of locating a sensor near the epicentre of a large magnitude EQ. Statistical analysis of the data may provide an important tool to address both of these problems, and a typical example for such statistical analyses is the cumulative probability plot for the ULF magnetic field[156]. This method is applied to the ULF data observed at Seikoshi station in the Izu peninsula during the period of July through December 1999[156]. They compared the fluctuation of the Seikoshi data with those sensors at Parkfield and Hollister, CA for the same period and with distribution function from a sensor at Corralitos, CA. The Corralitos data are from July to August prior to the Loma Prieta EQ (Figure 1 and Table1) and from November to December 1989 after the EQ. They found that the Seikoshi and pre-EQ Corralitos data have similar distribution functions and that Parkfield and Hollister have similar distributions. However, those from Seikoshi and Corralitos are signican-

ly higher below 50% cumulative probability than those from Parkfield and Hollister. They may have attributed this difference to an emission with a steep spectral slope, but with a narrow range magnetic field spectral density between 0.01Hz and 2 Hz.

## 4.4.2 Polarization analysis

As mentioned in section 4.1, the most important point for seismogenic ULF emissions is how to distinguish them from other various noises[157] and [57] proposed the so called polarization analysis, which measures the ratio of vertical magnetic field components to the horizontal components $S_Z/S_G$ ($S_G^2 = S_H^2 + S_D^2$ , H and D are two horizontal magnetic components and z, the vertical component). The principal idea of this polarization analysis is that while we expect that this ratio $S_Z/S_G$ (polarization) is relatively small for the geomagnetic variations (or geomagnetic pulsation) from the ionosphere/magnetosphere, this ratio is considered to be considerably enhanced, $S_Z/S_G \approx 1$ or even more for seismogenic emissions from the lithosphere by considering the Biot-Sarat's law by a possible current source.

This polarization analysis was successfully used for the 1993 Guam EQ [57] which showed an enhanced $S_Z/S_G$ during one month before the EQ, indicative of the presence of seismogenic ULF emissions. Then [17] studied the temporal evolution of $S_Z/S_G$ for the Kagoshima EQs, who found an enhancement of the polarization just before the EQ. Recently [158] have proposed an improved polarization method, which has enabled them to extract a ULF precursor to a moderate EQ in China.

## 4.4.3 Principal Component analysis

When we have the ULF data observed simultaneously at multiple stations, we can distinguish a few noise sources by use of principal component analysis. The principal component analysis was first applied to the ULF data during the Izu islands EQ swarm in 2000[16], because we have small arrays consisting of 3-4 magnetometers in

The Izu and Boso peninsulas. A remarkable event from the Kanto ULF network is the 2000 Izu islands EQ swarm. The seismic activity at Miyake Island started to be active in the late June of 2000, and the volcano eruption started there. The activity continued not only at Miyake Island, but also at its surroundings. By using the ULF data observed at close stations, for example in the Izu peninsula (Seikoshi, Mochikoshi, and Kamo), we can have three sets of data, which enables us to separate three possible sources. Generally speaking, the ULF signal observed at a station is a combination of a few effects: (1) geomagnetic variations of the magnetosphere (e.g., geomagnetic storms) due to the solar activity, (2) man-made noise, and (3) any other effect (including seismogenic emissions). The Eigen-values $\lambda_n$ (n=1, 2, 3) of the three principal components in the frequency range from T=10s to T=100s are traced by using the time-series data. The analysis shows that the first principal component ( $\lambda_1$) is highly correlated with the geomagnetic activity ($A_p$). The second Eigen-value

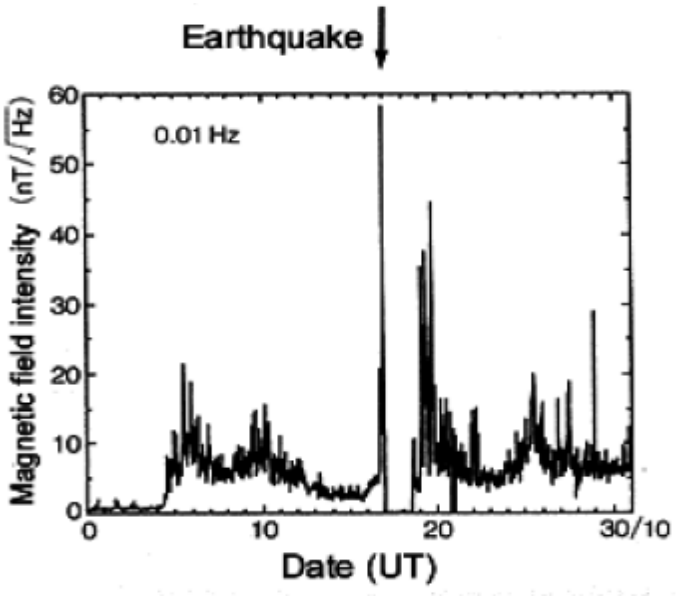


**Figure 4.4:** Temporal evolution of geomagnetic variation (only one horizontal component) for the Loma Prieta earthquake (f=0.01 Hz, 10 MHz) on October 18 1989 (after Fraser-Smith et al., 1990).

($\lambda_2$) is found to have a period of 24 hours, with daytime maximum and nighttime minimum. This suggests that this noise is due to the human activity. We notice an enhancement in $\lambda_3$ from the middle March to the middle June (about a few months), followed by a quiet period (about one week before the first EQ) and by a sharp increase a few days before the first EQ. Similar sharp peaks are seen for the subsequent EQs with magnitude greater than 6.0. This general behaviour seems to be in close agreement with Figure 4.4, which indicates that this variation is reflecting the crustal activity in this district[16].

### 4.4.4 Inter-station transfer function (ISTF) method

This method is an extension of the conventional transfer function, which is based on the comparison of the ULF data with those at a remote reference station located at a place with sufficiently low electromagnetic noise environment. By using the correlations of the variations at one current station with those at reference station, we will be able to eliminate first the global effect, (with the scale of hundreds of km) or local effect (less than few km), that is seismogenic effect[159].

[160] Have made full use of this ISTF method when analyzing the time dynamics of short- term variability of geoelectrical potential difference and geomagnetic fields observed at a few stations (Kiyosumi, Uchiura, and Fudago) located in the southern part of Boso peninsula, one of the most seismo active areas in Japan. Anomalous changes in electric and magnetic fields are observed in midnight on October 6 2002. The anomalous signals observed on October 6 are different from those originated from the train and other cultural noises on the basis of the study on the preferred directions of geoelectrical field. The investigation of simultaneous geomagnetic field changes suggests that the source of the change might be generated by an underground current because of the polarity patterns as observed at the above three stations.

## 4.5 Direction Finding

Direction finding is a sophisticated radio physical method to locate the ULF electromagnetic noise, that is, this technique is to estimate (one to infer) the position of radiating electromagnetic noise source by means of triangulation[161] . It is of extreme importance's to convince the people that the inferred position coincides with the epicentre of a future EQ. A few different principles are developed in the direction finding.

### 4.5.1 Magnetic Field Gradient Method

The direction finding based on the magnetic field gradient is applied to ULF emission for the above-mentioned Izu islands EQ swarm[162][163]. We have used the same local array network consisting of, at least, three stations in the Izu and Boso peninsulas. By measuring the gradient of the gradient of the horizontal and vertical components of the magnetic field at different frequencies and separating a few possible sources from their temporal changes with respect to the EQ time, we can deduces the direction of azimuth of the seismogenic noise as normal to the observed gradient. By plotting the distribution of signal azimuths, we perform the triangulation of the seismogenic ULF emission from the Izu and Bose peninsula data. Figure 5 is the final result, which indicates that the noise source seeming to be attributed to the EQ swarm is located at the place to be expected.

### 4.5.2 Goniometric Method

The goniometry is a conventional direction finding method[161] , in which we assume a linearly polarized electromagnetic field and the ratio of the amplitudes of two horizontal magnetic field and the ratio of amplitudes of two horizontal magnetic fields gives us the signal azimuth.

This method is applied to the ULF emissions for a recent large Niigata-Chuetsu EQ on 23 October, 2004 by using the data from other observatory at Nakatsugawa of the Chubu ULF/ELF network. The magnetitude and depth of this EQ are 6.8 and10 km. the three components of magnetic field ($B_x, B_y, B_z$) are measured at Nakatsugawa by using the same induction magnetometers like at Izu and Boso peninsulas, but the importantly different point is that the waveform measurement is being performed in wide frequency band with the sampling frequency of 100 Hz. By estimating the temporal evolution of magnetic intensity ( $B_y$ component) in the frequency range f <0.1 Hz, we estimate the period when the signal intensity is extremely enhanced by 3 dB as compared with the monthly means during several days from October 2 to October 6. This noise seems to be anomalous. However, we cannot conclude that this is associated with the EQ, even though it occurs about a few weeks before the EQ. Then, we performed the direction finding for this noise, and estimated the arrival azimuth by taking the ratio of $B_x/B_y$ for the emissions with anomalous amplitude during 2 to 6 October [164].

## 4.5.3 A new Polarization Ellipse Method

A new direction finding technique has been proposed by[165], which is an application of the polarization ellipse technique. The principle is as follows. The magnetic field components corresponding to the spectral bands dominated by seismo-electromagnetic fields define the polarization ellipse plane, which, at any instant, contains the source of electromagnetic fields. A line of intersection of such defined polarization ellipse planes for different observatories defines the source region.

This new direction finding has been applied to the ULF electromagnetic emissions observed at two distant stations in Koyna-Warna seismoactive region of Westindia[165]. They have succeeded in approximating the magnetic-dipole configuration for the source and magnetic field components along the intersection lines, and suggested the azimuth of the source is aligned in the NNW-SSE direction,

which is well coincident with the orientation of nodal plane of the normal fault mechanism for the two largest EQs recorded during the campaign.

## 5.6 Polarization Ellipse and Direction Finding

A useful analysis procedure has been presented by [166] by using the ULF-ELF data. The magnetic field variations are measured at the Karimshino observatory in Kamchatka, Russia since June 2000, and three magnetic field components are measured with the three-component magnetometers with sampling frequency of50 Hz. The power spectral densities are calculated for the field components (h, d and z components), together with the cross spectra of the horizontal components ($P_{hd}$). First, the periodograms of polarization ellipse for 256 point samples (~ 5 s) are calculated and then averaged over 30 min intervals. The parameters of polarization are estimated by the conventional procedure, such as ellipticity, sense of polarization, etc.

Based on the above analyses,[166] have found that a wide band emission was observed about 5 days before an EQ and lasted until five days after the EQ. Also, seismogenic ULF/ELF emission in the frequency range of 4-5 Hz are found to have an enhanced $P_{hh}/P_{dd}$ spectral ratio, a reduced standard deviation of ellipse orientation angle and the ellipticity and more linear polarization, as compared with the seismically quite background. Finally, the direction finding based on the analysis of the total field and its pulsed component has also been performed[166][167].

## 4.7 Fractal Analysis

This fractal analysis is one of physical processing methods in the sense that the non linear process taking place near the EQ hypocenter (i.e. self-organized criticality) can be studied as a change in fractal dimension and in fractal properties by means of the fractal analysis[168].

The fractal analysis has been applied to different EQ events. This fractal analysis was, for the first time, applied to the 1993 Guam EQ event, in which they measured the slopes of frequency spectra to deduce the fractional dimension[169]. This fractal result could support the occurrence of seismogenic ULF emission, and also it could provide us with the nonlinear self-organizing process in the lithosphere. The fractal properties for the 2000 Izu Island EQ swarm was studied by [170][171][172][173] have studied the monofractal and multi-fractal analyses for the 2003 Guam EQ. These fractal analyses are found to give a further support to the presence of seismogenic ULF emission and to be useful in investigating the nonlinear process of the lithosphere. This fractal analysis has been utilized for the analysis of different seismogenic effect[174].

# Chapter 5

## 5.0 Characteristics of Seismogenic ULF emissions

A large number of papers on seismogenic ULF emissions have been published since the famous EQs such as Spitak, Loma Prieta, and Guam. The characteristics of seismogenic Ulf emissions based on the results of above EQs and other such types of earthquakes are as;

(1) ULF electromagnetic emissions take place as a precursor to a relatively large EQ. The sensitivity distance (R) is 70-80 km for EQs with magnitude (M) 6.0, and about 100 km for (M) 7.0.

(2) The ULF emission for large EQs (with M> 6.0), seems to exhibit a typical temporal evolution. First of all we have a first peak one month to a few weeks before the EQ and a significant increase in amplitude a few days before the EQ. A slow relaxation is seen after the EQ.

(3) The amplitude of those seismogenic ULF emissions is found to range from 0.1 nT to a few nT. However, their frequency spectra are not well understood, that is what is the predominant frequency? Recent studies indicate the importance of the frequency of 10 mHz (period of 100s).

(4) There exist a few exceptions to the empirical threshold, including the case of the 2004 Niigata-Chuetsu EQ, the 2004 Sumatra EQ. The common property for these two EQs is their shallow depth (~10km). This can be understood in terms of the following hypothesis. Once the ULF emission is generated at shallow depths or just around the ground surface, they can propagate in the Earth-ionosphere waveguide over long distances as the quasi-TEM mode[164].

## 5.1 Future Direction on a Network of Magnetic Field Observations (Three Components)

In the future we will setup magnetic observatory in Jammu and Kashmir which is prone to EQs. Further we will use quartz sensors and other types of magnetometers like Fluxgate, induction coil proton precession to observe components of the magnetic field. in order to apply the magnetic field observation to earthquake prediction, it is desirable to (1) observe three components of the magnetic field, (2) sample the data, at least once per second , and (3) observe the magnetic field with resolution of less than 10 pp. Further, we have to be aware of other effects; we need information on the solar terrestrial effects (Geomagnetic variations, Geomagnetic storms) in the magnetic monitoring of seismic activity. Significant geomagnetic variations were observed before relatively large earthquakes. Thus it is quite necessary to estimate accurately the temporal/spatial characteristics of the signal by simultaneous monitoring of solar terrestrial effects from the ground and from space.

## 5.2 Conclusion

The seismogenic observations can be classified in to two types apart from the classification based on the direct and indirect measurements: (1) Local and (2) Integrated measurements[175]. The observation of seismogenic ULF emissions belongs to the first category, and the characteristic property of the local measurement is that the emissions in any frequency range can be detected only when our observing station happens to be close to the EQ epicentre. This is the reason why only 20-30 events are summarized in Figure 2.5. On the other hand, one typical example of the integrated measurement is the ionospheric perturbations by means of subionospheric VLF/LF signals. That is any Equation. Close to the great circle path from the transmitter to the receiver, so that it is rather easy for us to accumulate the number of events. In fact a significant statistical correlation between the VLF/LF propagation

anomaly (ionospheric perturbation) and EQs on the basis of many-years data has been established[176] . It is likely that distinct ULF emissions take place in the lithosphere in association with EQs, even though there have been published a few papers which may cast a question to the existence of seismogenic ULF emission[177 – 179]. The primary importance as for seismogenic ULF emissions is to increase the number of convincing events, though[180] has mentioned the presence of ULF emissions. In order to identify weak signals embedded in the noise, well sophisticated signal processing's are highly required. For this purpose we have to establish different scale network comprising of efficient magnetometers and digital processing systems. In this direction we establish a different-scale network in Jammu and Kashmir which would comprise of highly efficient magnetometers and quartz sensors. This would enable us to accumulate the number of events as well. Then we will use highly sophisticated signal processing's to identify the ULF signals.

# Bibliography


[1] Gokhberg M. B., Morgounov V. A. and Pokhotelov O. A. (1995). Reading Philadelphia, Gordon and Breach Science Publishers: 287.

[2] Molchanov O. A. (1994). Journal of Geophysical Research Letters **22**: 3091-3094.

[3] Aggarwal Y. P., Sykes L. R., Simpson D. W. and Richards D. G. (1975). J.Geophys. Res. Lett. **80**: 718-732.

[4] Nitsan U. (1977). J.Geophys. Res. Lett. **4**: 333-336.

[5] Yamada I., Matsuda K. and Mizutanni H. (1989). Phys. Earth Planet Int. **57**: 157-168.

[6] Gokhberg M. B., Morgounov V. A., Yoshino T. and Tomizawa I. (1982). J.Geophys. Res. Lett. **87**: 7824-7828.

[7] Fujinawa Y. and Takahashi K. (1990). Nature **347**: 376-378.

[8] Fraser-Smith A. C., Bernardi A., McGill P.R., Ladd M. E., Helliwell R. A. and Villard Jr A. D. (1990). J.Geophys. Res. Lett. **7**: 1465-1468.

[9] Kopytenko Y., Ismagilov V., Hayakawa M., Smirnova N., Troyan V. and Peterson T. (2001). Ann. Geofis **44**: 25-334.

[10] Molchanov O. A., Hayakawa M. and Rafalsky V. A. (1995). J.Geophys. Res. Lett. **100**: 1691-1712.

[11] Parrot M. (1994). Journal of Geophysical Research Letters **99:** 23339-23347.

[12] Parrot M. (1995). Adv. Space Research **15**: 1127-1135.

[13] Parrot M. (1993). J.Geophys. Res. Lett. **99:** 23339-23347.

[14] Kopytenko Y., Matiashvili T. G., Voronov P. M., Kopytenko F. A. and Molchanov O. A. (1990). Preprint of IZMIRAN, N3 (888).

[15] Hayakawa M., Kawate R., Molchanov O. A. and Kiyohumi Y. (1996). J.Geophys. Res. Lett. **23**: 241-244.

[16] Gotoh K., Akinaga Y., Hayakawa M. and Hattori K. (2002). J Atmos. Electr. **22**: 1-12.

[17] Hattori K., Akinaga Y., Hayakawa M., Yumoto K., Nagaos T. and Uyeda S. (2002): Hayakawa M. and Molchanov O. A. eds. Seismo Electromagnetics: Lithosphere-Atmosphere-Ionosphere Coupling. Terra Pub., Tokyo, 19-28.

[18] Kushwah V., Sing V. and Sing B. (2002). J. Ind. Geophys. Union **11**: 197-207.

[19] Bhattacharya S., Sarkar S., Gwal A. K. and Parrot M. (2002). Current Sciences **93**(1).

[20] Eftaxias K., Kaparis P., Olygiannakis J., Peratzakis A., Kopanas J.,Antonopoulos G. and Rigas D. (2003). Natural Hazards Earth System Sci. **3**:201-228.

[21] Molchanov O. A. and Hayakawa M. (1998). Phys. Of Earth Planet Int. **105**: 201-210.

[22] Matsu' ura M., Kataoko H. and Shibazaki B. (1992). Tectonophysics **211**: 135-148.

[23] Kamogawa M. and Ohtsuki Y. H. (1999). Proc. Japan Acad. Ser. B **75**(B)**:** 186-189.

[24] Ismaguilov V. S., Kopytenko Yu. A., Hattori K. and Hayakawa M. (2003). Natural Hazards Earth System Sci. **3**: 211-215.

[25] Huang Q. (2004). TAQ **15**(33): 469-491.

[26] Hayakawa M. and Hattori K. (2004). Inst. Electr. Engrs. Japan, Trans. Fundamentals and materials **124**: 1101-1108.

[27] Qian S., Hao J., Zhou J. and Gao J. (2002). Terra Pub. Co. Tokyo: 19-53.

[28] Ohta K., Watanable N. and Hayakawa M. (2005). Earth Planets Space **57**: 1103-1108.

[29] Schekotov A., Molchanov O. A., Yagova N., Fedorov E., Chebrov V., Sinitsin V., Gordeev E., Belyaev G. and Hayakawa M. (2006). Physics of Auroral Phenomena, Proc, XXIX Annual Seminar, Apatity: 161-164.

[30] Hayakawa M., Hattori K. and Ohta K. (2007). Sensors **7**: 1108-1122.

[31] Parrot M. et al. (1993). Phys. Earth Planet Int. **77**: 65-83.

[32] Fujinawa Y. and Takahashi K. (1994). Terra Sci. Pub. Co. Tokyo: 131.

[33] Hayakawa M. and Fujinawa Y. (1994). Terra Sci. Pub. Co. Tokyo.

[34] Parrot M., Berthelier J. J., Lebreton J. P., Sauvard J. A., Santolik O. and Bleeck J. (2006). Physics and Chemistry of the Earth **31**: 486-495.

[35] Davies K. and Baker D. M. (1965). J. Geophys. Res. **70**: 2251-2253.

[36] Moore G. W. (1964). Nature **203**: 508-509.

[37] Antselevich M. G. (1971). FAN Pub. Tashkent: 187-188.

[38] Sobolev G. A. and Husamiddinov S. S. (1985). Earthquake Prediction Res. **3**: 33-41.

[39] Fatkullin M. N., Zelenova T. I., Legen' ka A. D. (1989). Phys. Earth Planet. Int. **87**: 82.

[40] Pulinets S. A., Boyarchuk K. A., Lomonosov A. M., Khegai V. V. and Liu J. Y. (2006). Journal of Geomagnetism and Aeronomy **42**: 508- 513.

[41] Liu J. Y., Chen Y. I., Jhuang H. K. and Lin Y. H. (2004). TAQ **15**: 371-383.

[42] Rodger C. G., Dowden R. L. and Thomson N. R. (1996). J. Geophys. Res. Lett. **101**: 13369-13378.

[43] Pulinets S. A. (2004). TAQ **15**(3): 445-467.

[44] Boskova J., Shmilaur J., Jiricek F. and Triska P. (1993). J. Atmos. Terr. Phys **55**: 1689-1695.

[45] Parrot M. and Hobara. Y. (2005). J. Atmos. Sol-Terr. Phys. **67**: 677-685.

[46] Singh B., Kushwah V., Singh O. P., Lakshmi D. R. and Reddy B. M. (2004). Physics and Chemistry of Earth **29**: 537-550.

[47] Yuen P. F., Weaver P. F., Suzuki R. K. and Furumoto A. S. (1969). J. Geophys. Res. Lett. **74**: 2256-2264.

[48] Birfeld Y. G. (1973). Otkrytiya Izobret. Promyshl Obraztsy Tovarn. Znaki, No 42.

[49] Liperovsky V. A., Gladyshev V. A. and Shalimov S. L. (1991). Physics of Solid Earth **3**: 26-35.

[50] Shalimov S. L. and Gokhberg M. B. (1998). J. Earthquake. Pred. Res. **7**: 98-111.

[51] Hayakawa M. and Molchanov O. A. (2002). Terra Sci. Pub. Co. Tokyo: 11-55.

[52] Devi M., Barbara A. K. and Depueva A. (2004). Ann. Geophys **47**: 83-91.

[53] Chou Y. J., Liu J. Y., Pulinets S. A. and Chen Y. I. (200). Journal of Geodynamics **32**: 509-517.

[54] Dutta H. N., Dabas R. S., Rupesh M. D., Sharma K. and Singh B. (2007). International Journal of Remote Sensing **28**: 3141-3151.

[55] Fraser-Smith A. C., Bernardi A., McGill P. R., Ladd M. E., Helliwell R. A. and Villard Jr. O. G. (1990). Geophys. Res. Lett. **17**: 1465-1468.

[56] Molchanov O. A., Kopytenko Y. A., Voronov P. M., Kopytenko E. A., Matiashvili T. G., Fraser- Smith A. C., Bernadi A. (1992). Geophysics. Res. Lett. **19**: 1495-1498.

[57] Hayakawa M. Kawate R., Molchanov O. A. and Yumoto K. (1996).Geophys Res Lett **23**:241-244.

[58] Wilson E. (1922). Proc. R. Soc. A. **101**: 445-452.

[59] Kalashnikov A. C. and (1954). Trans Geofiz. Inst. Akad. Nauk. SSSR. Sb. Statei **25**:162-180.

[60] Stacey F. D. (1964). Pure. Appl. Geophys. **58**: 5-22.

[61] Stacey F. D., et al. (1965). Pure. Appl. Geophys. **62**: 96-104.

[62] Yamazaki Y. (1965). Bull. Earthq. Res. Inst. **44**: 783-802.

[63] Brace W. F. and Orange A. S. (1968a). J.Geophys. Res. **73**: 1443-1445.

[64] Brace W. F. and Orange A. S. (1968b). J.Geophys. Res. **73**: 5407-5420.

[65] Nagata T. (1969). Tectonophysics **21**: 427-445.

[66] Barsukov O. M. (1972). Tectonophysics **14**: 273-277.

[67] Rikitake T. (1968). Tectonophysics **6**: 59-68.

[68] Rikitake T. (1976). “Earthquake Prediction.” Elsevier.

[69] Honkura Y., et al. (1976). Tectonophysics **34**: 219-230.

[70] Fitterman D. V. (1979). J.Geophys. Res. **84**: 6031-6040.

[71] Fitterman D. V. (1981). J.Geophys. Res. **86**: 9585-9588.

[72] Ishido T. and Mizutani M. (1981). J.Geophys. Res. **86**: 1763-1775.

[73] Varotsos P. and Alexopoulos K. (1987).Tectonophysics **136**: 355-339.

[74] Dobrovolsky I. P., et al. (1989). Phys. Earth Planet. Inter**. 57**: 144-156.

[75] Sasai Y. (1980). Bull. Earthq. Res. Inst. **55**: 387-447.

[76] Sasai Y. (1991a). Bull. Earthq. Res. Inst. **43**: 21-64.

[77] Sasai Y. (1991b). Bull. Earthq. Res. Inst. **66**: 585-722.

[78 ] Park S. K. (1991). J. Geophys. Res. **96**: 14211-14237.

[79] Fujinawa Y., et al. (1992). Geophys Res. Lett. **19**: 9-12.

[80 ] Fenoglio M. A., et al. (1995). J.Geophys. Res. **100**: 12951-12958.

[81] Utada H. (1993). Tectonophysics **224**: 149-152.

[82] Mizutani H. and Ishido T. (1996). J. Geomagn. Geoelectr. **28**: 179-188.

[83] Fitterman D. V. (1978). J.Geophys. Res. **83**: 5923-5928.

[84] Johnston M. J. S., et al. (1987). Tectonophysics **144**: 189-206.

[85] Nourbehecht B. (1963). PhD. Thesis. Massachussetts Institute of Technology. Cambridge.

[86] Williamson S. J. and Kaufman L. (1981). J. Magn. Mater. **22**: 129-201.

[87] Ahmad M. (1964). Geophys. Prospect **12**: 49-64.

[88] Kalashnikov A. C. and Kapitsa S. P. (1952). Proc. Acad. Sci. USSR **86**: 521-523.

[89] Kapitsa S. P. (1955). Izv. Akad. Nank. SSSR. Ser. Geofiz **6**: 489-504.

[90] Ohnaka M. and Kinoshita H. (1986). J. Geomagn. Geoelectr. **20**: 93-99.

[91] Kean W. F., et al. (1976). J.Geophys. Res. **85**: 861-872.

[92] Revol J., et al. (1977). Earth Planet. Sci. Lett. **37**: 296-306.

[93] Martin III. R. J. (1980). J. Geomagn. Geoelectr. **32**: 741-755**.**

[94] Pike S. J., et al. (1981). J.Geophys. Res.**33**: 449-466.

[95] Stacey F. D. (1962). Philos. Mag. **7**: 551-556.

[96] Stacey F. D. and Johnston M. J. S. (1972). Pure. Appl. Geophys. **97**: 146-155.

[97 ] Kern J. w. (1961). J.Geophys. Res. **66**: 3801-3805.

[98] Shami S. and Stacey F. D. (1969). Bull. Seismol. Soc. Am. **59**: 1435-1448.

[99 ] Johnston M. J. S. (1978). J. Geomagn. Geoelectr. **30**: 511-522.

[100] Davis P. M., et al (1979). Phys. Earth Planet. Inter. **19**: 331-336.

[101 ] Sasai Y. (1983). Bull. Earthq. Res. Inst. **58**: 763-785.

[102 ] Davis P. M., et al. (1984). Geophys. Res. Lett. **11**: 225-228.

[103 ] Johnston M. J. S., et al. (1994). Bull. Seismol. Soc. Am. **84**:792-798.

[104 ] Banks P. O., et al. (1991). J.Geophys. Res**. 96**: 21575-21582.

[105 ] Sasai Y. (1994). Geomagn. Geoelectr. **42**: 329-340.

[106 ] Brace W. F., et al. (1965). J.Geophys. Res. **70**: 5669-5678.

[107] Brace W. F. (1975). Pure Appl. Geophys. **113**:207-217.

[108 ] Lockner D. A. and Byerlee J. D. (1968). Pure Appl. Geophys. **124**: 659-676.

[109 ] Park S. K., et al. (1993). Rev. Geophys. **31**: 117-132.

[110 ] Fitterman D. V. and Madden T. R. (1977). J. Geophys. Res. **82**: 5401-5408.

[111 ] Gamble T. D., et al (1979). Geophysics **44**: 53-58.

[112 ] Madden T. R., et al. (1993). J. Geophys. Res. **98**: 795-808.

[113 ] Finkelstein D., et al. (1973). J. Geophys. Res.**78**: 992-993.

[114] Baird G. A. and Kennan P. S. (1985). Tectonophysics **111**: 147-154.

[115] Lowell F. And Rose-Innes A. C. (1986). Adv. Phys. **29**: 947-1023.

[116 ] Gokhberg M. B., et al. (1982). J. Geophys. Res. **87**: 7824-7828.

[117 ] Brady B. T. (1992). In: "Report 92-15, IGPP," University of California, Riverside.

[118 ] Blanchard D. C. (1964). Nature **201**: 1164-1166.

[119 ] Matteson M. J. (1971). J. Colloid. Interface Sci. **37**: 879-890.

[120 ] Chalmers A. (1976). "Atmospheric Electricity," Prergamon.

[121 ] Dologlou Revelioti E. and Varotsos P. (1986). Geophysics. **59**: 177-182.

[122 ] Freund F., et al. (1992). In: "Report 92-15, igpp." University of California, Riverside.

[123 ] Tunck G. T., et al. (1977). Tectonophysics **39**: 149-152.

[124 ] Sasaoka H., et al. (1988). Geophys. Res. Lett. **25**: 2225-2228.

[125] Warwick J. W., et al. (1982). J. Geophys. Res. **87**: 2851-2859.

[126 ] Lockner D. A. and Byerlee J. D. (1986). Pure Apple. Geophys. **124**: 659-676.

[127 ] Honkura Y. and Kuwata Y. (1993). Tectonophysics **224**: 257-264.

[128 ] Lockner D. A., et al.(1991). Nature **350**: 39-42.

[129 ] Shercliff J. A. (1965). "A Textbook of Magneto hydrodynamics," Pergamon Press.

[130 ] Brace W. F. (1980). Int. J. Rock Mech. **17**: 876-893.

[131] Fracer D. C. (1966). Geophys. J. R. Astron. Soc. **11**: 507-517.

[132 ] Stacy F. D. and Banerjee S. K. (1974). "The Physics Principles of Rock Magnetism." Elsevier.

[133 ] Stacy F. D. (1992). "Physics of the Earth." 3rd edn. Brookfield Press.

[134] Rikitake T. and Yakoyama (1955). ). J. Geophys. Res. **60**:165-172.

[135] Hurst A. W. and Christoffel D. A. (1973). NZ J. Geol. Geophysics. **16**: 965-972.

[136] Emeleus T. G. (1977). J. Volc. Geotherm. Res. **2**: 343-359.

[137] Zlotnicki J. and Le Mouel J. L. (1988). J. Geophys. Res. **93**: 9157-9171.

[138 ] Hamano Y., et al. (1989). J. Geomagn. Geoelectric. **41**: 203-220.

[139 ] Dzurisin D., et al. (1990). Bull. Seismol. Soc. Am**. 95**:2763-2780.

[140] Zlotnicki J. and Le Mouel J. L. (1990). Nature **343**: 633-636.

[141] Tanaka Y. (1993). J. Volc. Geotherm. Res. **56**: 319-328.

[142] Tanaka Y. (1995). J. Geomagn Geoelectr. **47**: 325-336.

[143] Lion K.S. (1959). Instrumentation in Scientific Research, Electrical Input Transducers, New York: McGraw Hill.

[144] Everett H. R. (1995). Sensor for Mobil Robots: Theory and Application, Wellesy,

[145] Lenz J. E. (1990). A review of magnetic sensors, Proc. of IEEE **78**: 973-989**.**

[146] Farthing W. H. and Folz W. C. (1967). Rev. Sci. Instrum **38**: 1023-1030.

[147] Hartmann F. (1972). IEEE Trans. Magnetics. MAG **8**: 66-75.

[148] Wellstood F., Heiden C. and Clark J. (1984). Rev. Sci.Instrum. **66**: 952-957.

[149] Primdahi F. (1979). J. Phys. E. Sci. Instrum. **1**: 242-253.

[150] Pelterin C.J. and Acuna M. H. (1970). NASA Technical Note, TN D-5325.

[151] Marshall S. V. (1971). IEEE Trans. Magnetics. MAG **7**: 183-185.

[152] Geyger W. A. (1964). Nonlinear-Magnetic Control Devices, New York: McGraw-Hill.

[153] Cohen D. (1975). IEEE Trans. Magnetics, MAG **11**: 694-700.

[154] Falco C. M. and Schuller I. K. (1981). SQUID Applications to Geophys, The Society of Exploration Geophysicists 13-18.

[155] Clark J. (1994). SQUIDs. Sci. Am. 46-53.

[156] Koons H. C., Roedger J. L., Hobara Y., Hayakawa M. and Fraser-Smith A. C. (2002). In: Hayakawa M and Molchanov O A eds. Seismo Electromagnetics: Lithosphere-Atmosphere-Ionosphere Coupling. TERRAPUB, Tokyo, 29-39.

[157] Kopytenko Yu. A., Matiashvili T. G., Voronov P. M., Kopytenko E. A. and Molchanov O. A. (1993). Phys Earth Planet Inter **77**: 84-95.

[158] Ida Y., Yang D., Li Q., Sun H. and Hayakawa M. (2008). Natural Hazards Earth System Sci **8**:775-777.

[159] Hattori K. (2004). Terr Atmos Ocean Sci **15**: 329-360.

[160] Takahashi I., Hattori K., Harada M., Yoshino C. and Isezaki N. (2007). Ann Geophys (Italy) **50**: 123-135.

[161] Hayakawa M. and Ohta K. (2006). IEEJ Trans Fundamentals and Materials **126**(2): 65-70.

[162] Kopytenko Yu. A., Ismaguilov V. S., Hattori K. and Hayakawa M. (2002). In: Hayakawa M. and Molchanov O. A. eds. Seismo Electromagnetics: Lithosphere-Atmosphere-Ionosphere Coupling. TERRAPUB, Tokyo, 11-18.

[163] Ismaguilov V. S., Kopytenko Yu. A., Hattori K. and Hayakawa M. (2002). Natural Hazards Earth System Sci **20**: 1-5.

[164] Ohta K., Watanabe N. and Hayakawa M. (2007). Int'l J Remote Sensing **28**: 3121-3131.

[165] Dudkin F., Rawat G., Arora B. R., Korepanov V., Leotyena O., and Sharma A. K. (2010). Natural Hazards Earth System Sci **10:** 1-10.

[166] Schekotov A. Y., Molchanov O. A., Hayakawa M., Fedorov E. N., Chebrov V. N., Sinitsin V. I., Gordeev E. E., Belyaev G. G. and Yagova N. V. (2007). Radio Sci **42**: RS6S90, doi: 10. 1029/2005RS003441.

[167] Schekotov A. Y., Molchanov O. A., Hayakawa M., Fedorov E. N., Chebrov V. N., Sinitsin V. I., Gordeev E. E., Andreevsky S. E., Belyaev G. G., Yagova N. V., Gladishev V. A., and Baransky L. N. (2008). Natural Hazards Earth System Sci **8**: 1237-1242.

[168] Hayakawa M., Ida Y.(2008). Current Development in Theory and Applications of Wavelets **2**(2): 159-174.

[169] Hayakawa M., ed. (1999). Terra Scientific Pub. Comp., Tokyo, 996pp.

[170] Gotoh K., Hayakawa M., Smirnova N. A., and Hattori K. (2004). Phys Chem. Earth **29**: 419-424.

[171] Smirnova N., Hayakawa M. and Gotoh K. (2004). Phys Chem. Earth **29**: 445-451.

[172] Ida Y., Hayakawa M., Adalev A. and Gotoh K. (2005). Natural Hazards Earth System Sci **8**:775-777.

[173] Ida Y., Hayakawa M. (2006). Nonlinear Processes Geo-phys **12**: 409-412.

[174] Eftaxias K., Kapiris P., Dologlou E., Kopanas J., Bogris (2002). Geophys Res Lett **29**, doi: 10.1029/2001GL013786.

[175] Molchanov O. A. and Hayakawa M. (2008). TERRAPUB, Tokyo, 189pp.

[176] Hayakawa M. And Hobara Y. (2010). Geomagnetic, Natural Hazards and Risk **1**(2): 115-155.

[177] Campbell W. H. (2009). J. Geophysics. Res. **114**: A05307, doi: 10, 1029/2008JA013932.

[178] Thomas J. N., Love J. J. And Johnson M. J. S. (2009a). Phys Earth Planet Inter 173:207-215, doi 10, 1016/J. Pepi2008.11.014.

[179] Thomas J. N., Love J. J., Johnson M. J. S. And Yumoto K. (2009b). Geophysics Res. Lett. **36**: L16301, doi:1029/2009 GL039020.

[180] Fraser-Smith A. C. (2009). Tran world Research Network, Trivandrum (India), Chapter 1, 1-20.